arXiv:2007.06976v2 [physics.plasm-ph] 31 Mar 2021

Inverse cascade and magnetic vortices in kinetic Alfvén-wave turbulence

G. Miloshevich, D. Laveder, T. Passot, P.L. Sulem

Université Côte d'Azur, CNRS, Observatoire de la Côte d'Azur, Laboratoire J.L. Lagrange, Boulevard de l'Observatoire, CS 34229, 06304 Nice Cedex 4, France

(Received xx; revised xx; accepted xx)

A Hamiltonian two-field gyrofluid model for kinetic Alfvén waves (KAWs) in a magnetized electron-proton plasma, retaining ion finite-Larmor-radius corrections and parallel magnetic field fluctuations, is used to study the inverse cascades that develop when turbulence is randomly driven at sub-ion scales. In the directions perpendicular to the ambient field, the dynamics of the cascade turns out to be nonlocal and the ratio χ_f of the wave period to the characteristic nonlinear time at the driving scale affect some of its properties. For example, at small values of χ_f, parametric decay instability of the modes driven by the forcing can develop, enhancing for a while inverse transfers. The balanced state, obtained at early time when the two counter-propagating waves are equally driven, also becomes unstable at small χ_f, leading to an inverse cascade. For β_e smaller than a few units, the cascade slows down when reaching the low-dispersion spectral range. For higher β_e, the ratio of the KAW to the Alfvén frequencies displays a local minimum. At the corresponding transverse wavenumber, a condensate is formed, and the cascade towards larger scales is then inhibited. Depending on the parameters, a parallel inverse cascade can develop, enhancing the elongation of the ion-scale magnetic vortices that generically form.

1. Introduction

Large-scale magnetic structures are commonly observed in astrophysical media and have also been shown to stabilize the H mode in tokamaks (Solano *et al.* 2010). The question then arises as to what are the physical processes contributing to their formation and prescribing their characteristic size. In astrophysics, among the potential mechanisms, turbulent inverse cascades have been suggested. In this context, special attention was paid in the literature to the cascade of magnetic helicity in the framework of incompressible magnetohydrodynamics (MHD) in the absence of an ambient field (Frisch *et al.* 1975; Pouquet *et al.* 1976; Meneguzzi *et al.* 1981; Alexakis *et al.* 2006; Müller *et al.* 2012; Linkmann & Dallas 2016, 2017; Pouquet *et al.* 2019). Extension to compressible MHD with Mach number that goes up to unity (Balsara & Pouquet 1999; Brandenburg 2001), as well as the case of incompressible Hall-MHD (Pouquet *et al.* 2020) were also studied. The cascade is however prevented by the presence of an ambient field, due to the non-conservation of the magnetic helicity based on the fluctuations, and due to the lack of gauge-invariance of the conserved generalized magnetic helicity that can be defined in this regime (Matthaeus & Goldstein 1982; Stribling *et al.* 1994; Brandenburg & Matthaeus 2004). Conservation of the magnetic helicity together with the existence of an inverse cascade (Kim & Cho 2015) are nevertheless recovered in electron magnetohydrodynamics (EMHD) that describes whistler waves at electron scales where the ion motion is negligible and the dispersion associated with the Hall effect is significant.

One is thus naturally led to wonder about the possibility of the existence of an inverse cascade for kinetic Alfvén waves (KAWs) at sub-ion scales.

A question arises concerning the possible drivers for such inverse cascades. Bypassing the classical local direct cascade, energy could be directly injected at small scales via nonlocal interactions mediated by magnetic reconnection occurring in thin ion-scale current sheets. It has recently been proposed that these reconnection events could generate an inverse flux toward larger scales, as well as starting a transfer of energy toward smaller scales (Franci *et al.* 2017). Another example of possible mechanism was discussed in the context of Alfvenic turbulence in the distant ion foreshock region where observation of an inverse cascade was reported, related to the existence of nonlinear parametric instabilities generated by upstream accelerated protons reflected on the bow shock (He *et al.* 2019).

The dynamics of a strongly magnetized plasma characterized by small perturbations of a homogeneous equilibrium is appropriately described by the gyrokinetic formalism, from which reduced gyrofluid models of various complexity can be derived. Such models can provide a uniform description covering a spectral range extending from MHD to electron scales. They capture the transition from Alfvén waves to KAWs, which are known to play a dominant role in the solar wind at MHD (Belcher & Davis 1971; Réville *et al.* 2020) and sub-ion (Alexandrova *et al.* 2009; Sahraoui *et al.* 2010; Salem *et al.* 2012; Podesta 2013) scales, respectively. Their nonlinear dynamics is isolated in the description provided by a reduced two-field gyrofluid model discussed in Passot *et al.* (2018); Passot & Sulem (2019); Miloshevich *et al.* (2019). When neglecting electron inertia, it extends to finite beta parameters the model considered in Zocco & Schekochihin (2011) taken in the isothermal limit, retaining the coupling to the parallel magnetic fluctuations.

Kinetic effects, such as Landau damping, cyclotron resonance or micro-instabilities are definitely not taken into account in the two-fluid gyrofluid model. The coupling to magnetosonic waves, which could play a role at larger scales (e.g. they permit the decay instability of Alfvén waves at MHD scales) is also not retained. Nevertheless, the two-field gyrofluid model enables the study (for a broad range of plasma parameters) of imbalanced turbulence, characterized by an excess of the energy carried by one of the two types of counter-propagating waves. Imbalanced Alfvénic turbulence is ubiquitous in the solar wind (Tu *et al.* 1989; Lucek & Balogh 1998; Wicks *et al.* 2013), with the degree of imbalance dependent on the type of wind (Tu *et al.* 1990; Bruno *et al.* 2014; Bruno *et al.* 2017; D'Amicis *et al.* 2019) and of the distance from the Sun (Roberts *et al.* 1987; Marsch & Tu 1990; Chen *et al.* 2020). In the framework of the two-field model, imbalance is easily characterized by the generalized cross-helicity (GCH) which is an ideal quadratic invariant that reduces to the negative cross-helicity at the MHD scales and to the magnetic helicity at the sub-ion scales. When turbulence is driven by injection of energy and of GCH, these quantities are expected to cascade forward to the smaller scales and/or backward to the larger ones, depending in particular on the injection scale compared to the ion Larmor radius (or the sonic Larmor radius). Indeed, no inverse cascade can take place at the MHD scales in the presence of a strong ambient field, while an inverse cascade of magnetic helicity was predicted in the (dispersive) sub-ion range, by analogy with EMHD (Schekochihin *et al.* 2009), and also on the basis of absolute equilibrium arguments (Passot *et al.* 2018). Based on these observations, one expects that as the inverse cascade approaches the MHD scales, its properties will be significantly affected.

In addition to providing a mechanism for the formation of large-scale structures in fluids and plasmas, inverse cascades can reveal various interesting phenomena, like critical transitions that are observed in split-cascade configurations when the relevant

dimensionless parameter is varied (Alexakis & Biferale 2018). This includes transitions from inverse to forward cascade of energy in thin-layer turbulence (Benavides & Alexakis 2017) and transitions from MHD to fluid turbulence, when the relative strength of the magnetic forcing parameter is varied (Seshasayanan *et al.* 2014). Furthermore, there are examples of such criticality in rotating and stratified flows where helicity conservation can be broken when dynamical parameters such as Rossby and Froude numbers are varied (Marino *et al.* 2013).

The present paper addresses the existence and the properties of the inverse cascades which can develop in the two-field gyrofluid model when energy and GCH are injected. We will vary the injection rate, the driving scale and the ratio β_e of equilibrium electron thermal pressure to the magnetic pressure due to the ambient field, and suggest that the ratio χ_f of the wave period to the characteristic nonlinear time at the driving scale affects some properties of the inverse cascade in the transverse spectral plane (e.g. its "degree of self-similarity"), at least at early time. At late times, the properties of the cascade appear to be rather dependent on the driving scale and β_e. Section 2 provides a description of the model, together with a brief discussion of the Fjørtoft argument often used for predicting the existence of an inverse cascade. Section 3 specifies the numerical set up and the conditions of the simulations. Section 4 discusses the global properties of the cascade dynamics in the context of our fiducial simulation where turbulence is driven far into the sub-ion range. Section 5 addresses the effect of the turbulence strength on the early dynamics, and in particular the transition from a self-similar spectrum to a propagating spectral bump, the emergence of the parametric decay instability or the instability of balanced turbulence, as the amplitude of the magnetic fluctuations is reduced. Section 6 addresses the situation where the cascade reaches the weakly dispersive range. Section 7 is concerned with the arrest of the cascade and the generation of a finite-scale condensate, when β_e is large enough. The coherent structures, in the form of magnetic vortices that are generated in physical space as consequences of the inverse cascades and of their arrest, are described in Section 8. Section 9 is the Conclusion. The Appendices include a brief description of the decay instability in the context of the present model and the derivation of the shell-to-shell transfers.

2. The two-field gyrofluid model

2.1. *Equations and conservation laws*

A description of the Alfvén wave dynamics from the MHD to the electron scales, in an electron-proton plasma, is provided by the two-field gyrofluid model which involves the gyrokinetic scaling corresponding to a strong spectral anisotropy and weak nonlinearity. In the absence of dissipation and driving, it involves two equations for the electron gyrocenter number density N_e and the parallel† component of the magnetic potential

† At the order at which the equations are considered, parallel or longitudinal refers to the direction of the ambient field, except in the case of the parallel derivative $\nabla_\parallel$ where the derivative is taken in the direction of the local magnetic field.

$A_\parallel$, in the form‡

$$\partial_t N_e + [\varphi, N_e] - [B_z, N_e] + \frac{2}{\beta_e}\nabla_\parallel \Delta_\perp A_\parallel = 0 \tag{2.1}$$

$$\partial_t L_e A_\parallel - \left[\varphi, \frac{2\delta^2}{\beta_e}\Delta_\perp A_\parallel\right] + \left[B_z, \frac{2\delta^2}{\beta_e}\Delta_\perp A_\parallel\right] + \nabla_\parallel(\varphi - N_e - B_z) = 0. \tag{2.2}$$

In the above equations, the parallel magnetic fluctuations B_z and the electron gyrocenter number density N_e are related to the electric potential φ by $B_z = M_1\varphi$ and $N_e = -M_2\varphi$, where M_1 and M_2 are Fourier multiplier operators written as $M_1 = L_1^{-1}L_2$ and $M_2 = L_3 + L_4L_1^{-1}L_2$ (here, $\delta^2 = m_e/m_i$ denotes the electron to proton mass ratio), the operators L_i being defined as

$$L_1 = \frac{2}{\beta_e} + (1+2\tau)(\Gamma_0 - \Gamma_1) \tag{2.3}$$

$$L_2 = 1 + \frac{1-\Gamma_0}{\tau} - \Gamma_0 + \Gamma_1 \tag{2.4}$$

$$L_3 = \frac{1-\Gamma_0}{\tau} - \delta^2\Delta_\perp \tag{2.5}$$

$$L_4 = 1 - \Gamma_0 + \Gamma_1 \tag{2.6}$$

$$L_e = 1 - \frac{2\delta^2}{\beta_e}\Delta_\perp. \tag{2.7}$$

Here, $\Delta_\perp = \partial_{xx} + \partial_{yy}$ is the Laplacian in the plane transverse to the ambient field and $[f, g] = \partial_x f \partial_y g - \partial_y f \partial_x g$ the canonical bracket of two scalar functions f and g. Furthermore, Γ_n denotes the (nonlocal) operator $\Gamma_n(-\tau\Delta_\perp)$ associated with the Fourier multiplier $\Gamma_n(\tau k_\perp^2)$, defined by $\Gamma_n(x) = I_n(x)e^{-x}$ where I_n is the modified Bessel function of first type of order. Furthermore,τ denotes the ratio of the proton to the electron temperatures at equilibrium. For a scalar function f, the parallel gradient operator $\nabla_\parallel$ is defined by

$$\nabla_\parallel f = -[A_\parallel, f] + \frac{\partial f}{\partial z}. \tag{2.8}$$

One recovers the fluctuating magnetic field from the expression of B_z given above and $\boldsymbol{B}_\perp = \nabla_\perp \times (A_\parallel \widehat{\boldsymbol{z}})$.

Characterizing the plasma equilibrium state by the number density n_0, the temperatures T_{i0} and T_{e0}, and the ambient field B_0, the model is written above in a non-dimensional form, using the following units: time is normalized to the inverse ion gyrofrequency $\Omega_i^{-1} = (eB_0/(m_i c))^{1/2}$ (where e is the proton charge and c the speed of light), lengths by the sonic Larmor radius $\rho_s = c_s/\Omega_i$ where $c_s = \sqrt{T_{e0}/m_i}$ is the sound speed. Thus wavenumbers and wavevector components are measured in units of ρ_s^{-1}. The other normalization factors include B_0 for the parallel magnetic fluctuations B_z, $B_0\rho_s$ for the parallel magnetic potential $A_\parallel$, the equilibrium number density n_0 for the electron gyrocenter density N_e and T_e/e for the electric potential φ. Furthermore,

‡ In Eq. (2.2), the term $[B_z, (2\delta^2/\beta_e)\Delta A_\parallel]$ is subdominant within the asymptotics leading to the model, but as mentioned in Passot *et al.* (2018), this term is retained in order to preserve the Hamiltonian structure, which is an important property of the model in the sense that it ensures the absence of uncontrolled dissipation. The second term in the rhs of Eq. (2.5) is also subdominant but has been retained as it becomes relevant when β_i becomes of order unity. This term is needed to recover the system of equations governing inertial kinetic Alfvén waves with $\tau \gg 1$ (see also Chen & Boldyrev (2017)). The effect of subdominant terms will only be significant on a time much longer than the time interval for which the asymptotic model is valid.

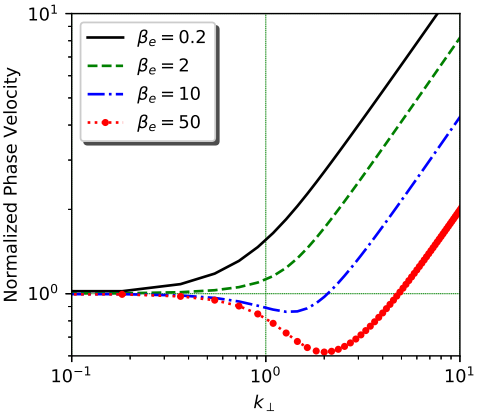


Figure 1: Normalized parallel-phase velocity $v_{ph}\sqrt{\frac{\beta_e}{2}}$ (or equivalently, ratio of the KAW frequency $v_{ph}k_\parallel$ to the Alfvén frequency $v_A k_\parallel$), versus the transverse wavenumber $k_\perp$ for various values of β_e.

the parameter $\beta_e = 8\pi n_0 T_{e0}/B_0^2$ is the ratio of the equilibrium electron pressure to the magnetic pressure due to the ambient field.

At the level of the linear approximation, the KAW parallel-phase velocity $v_{ph} = \omega/k_z$ is given by

$$v_{ph}^2 \equiv \left(\frac{\omega}{k_z}\right)^2 = s^2 \frac{k_\perp^2}{1 + \frac{2\delta^2 k_\perp^2}{\beta_e}} \frac{1 - \widehat{M}_1 + \widehat{M}_2}{\widehat{M}_2}, \tag{2.9}$$

where the hat refers to the Fourier symbol of the operator and $s = (2/\beta_e)^{1/2}$ is the Alfvén velocity v_A measured in sound speed units ($s = v_A/c_s$). We plot in Fig. 1 v_{ph}/s, versus the transverse wavenumber $k_\perp$, when electron inertia is neglected. For all values of β_e, the ratio v_{ph}/s, that can also be viewed as the wave frequency normalized by the Alfvén wave frequency $v_A k_\parallel$, is asymptotically equal to unity at large scale (dispersionless limit). On the other hand, while for small ($\beta_e = 0.2$) or moderate ($\beta_e = 2$) values of the electron beta parameter, v_{ph}/s involves a monotonic transition to a $k_\perp$-scaling at sub-ion scales, for larger β_e (e.g. 10 or 50), it displays a local minimum at a wavenumber that (in inverse sonic Larmor radius units) increases with β_e at fixed τ and only depends on β_i when measured in units of the ion Larmor radius ρ_i. A similar behaviour is observed in Fig. 3 ($\tau = 100$) and 5 ($\tau = 1$) of Howes *et al.* (2006) where this quantity, is computed from the gyrokinetic theory and also in the framework of the full linear kinetic theory taken in the quasi-transverse limit. As discussed below, it turns out that the sensitivity of the dispersion to the transverse wavenumber, as measured by the parallel-phase velocity v_{ph}, has an important effect on the nonlinear dynamics of the cascade. In particular, it has an impact on the generation of a finite-size condensate and on the formation of large-scale coherent structures.

In physical space, the eigenmodes, which can be referred to as Elsasser potentials, are given by

$$\mu^\pm = \Lambda\varphi \pm sA_\parallel, \tag{2.10}$$

where

$$\Lambda = D_e^{-1}(1 + M_2 - M_1)^{1/2} M_2^{1/2}, \tag{2.11}$$

with $D_e^2 = (-\Delta_\perp)L_e$. They obey

$$\begin{aligned}
&\partial_t \mu^\pm \pm V_{ph}\partial_z \mu^\pm \\
&+\frac{1}{4}\Lambda^{-1}D_e^{-2}M_3\Big\{[\Lambda^{-1}M_3(\mu^+ + \mu^-), \Lambda^{-1}M_2(\mu^+ + \mu^-)] + [(\mu^+ - \mu^-), \Delta_\perp(\mu^+ - \mu^-)]\Big\} \\
&\pm\frac{1}{4}D_e^{-2}\Delta_\perp\Big\{[(\mu^+ - \mu^-), \Lambda^{-1}M_2(\mu^+ + \mu^-)] + [L_e(\mu^+ - \mu^-), \Lambda^{-1}(1 - M_1)(\mu^+ + \mu^-)]\Big\} = 0.
\end{aligned} \tag{2.12}$$

The systems (2.1)-(2.2) or (2.12) preserve the energy $\mathcal{E}$ and the generalized cross-helicity $\mathcal{C}$, defined as

$$\begin{aligned}
\mathcal{E} &= \frac{1}{2}\int \Big(\frac{2}{\beta_e}|\nabla_\perp A_\parallel|^2 + \frac{4\delta^2}{\beta_e^2}|\Delta_\perp A_\parallel|^2 - N_e(\varphi - N_e - B_z)\Big)d^3x \\
&= \frac{1}{4}\int \left\{(D_e\mu^+)^2 + (D_e\mu^-)^2\right\} d^3x. \qquad (2.13)\\
\mathcal{C} &= -\int N_e\Big(1 - \frac{2\delta^2}{\beta_e}\Delta_\perp\Big)A_\parallel d^3x. \\
&= \frac{1}{4}\int \left\{\left(V_{ph}^{-1/2}D_e\mu^+\right)^2 - \left(V_{ph}^{-1/2}D_e\mu^-\right)^2\right\} d^3x, \qquad (2.14)
\end{aligned}$$

where V_{ph} is the operator in physical space, which in Fourier space corresponds to the multiplication by v_{ph}. Note that $\mathcal{C}$ was defined with an opposite sign in Passot *et al.* (2018).

2.2. *Normal-field formulation*

As is common with noncanonical Hamiltonian systems, the associated Poisson bracket possesses Casimir invariants, corresponding to $C_\pm = \int G^\pm d^3x$, where $G^\pm = L_e A_\parallel \pm \delta N_e$ are referred to as normal fields. In terms of these fields, the two-field gyrofluid model can be rewritten in the form

$$\partial_t G^\pm + [\varphi^\pm, G^\pm] + \partial_z\left(\varphi^\pm \mp \frac{1}{\delta}G^\pm\right) = 0, \tag{2.15}$$

where $\varphi^\pm = \varphi - B_z \pm \frac{1}{\delta}A_\parallel$. In terms of these variables, GCH simply reads

$$\mathcal{C} = -\frac{1}{4\delta}\int \left\{(G^+)^2 - (G^-)^2\right\} d^3x. \tag{2.16}$$

Similarly,

$$\mathcal{E} = \frac{1}{2}\int \left\{\frac{1}{2\beta_e}L_e^{-1}|\nabla_\perp(G^+ + G^-)|^2 + \frac{1}{4\delta^2}M_3M_2^{-1}(G^+ - G^-)^2\right\} d^3x. \tag{2.17}$$

Note that the system of equations (2.15) for $G^\pm$ becomes degenerate in the limit $\delta \to 0$, as the two equations become identical and reproduce the equation for $A_\parallel$. The equation for N_e corresponds to the first order in a development in δ^2. As seen below, this formulation nevertheless has a major interest for estimating the energy and GCH spectral transfers estimated in Appendix B.

2.3. *Fjørtoft argument for an inverse cascade*

The Fjørtoft (1953) argument originally refers to a simple method to predict the existence of an inverse cascade by noting the impossibility of simultaneous direct cascades

of two ideal invariants whose spectra differ by a power of the wavenumber. Other versions of the argument can be found in Nazarenko (2011) (and references therin). We will first revisit the use of the Fjørtoft (1953) argument to support the existence of an inverse GCH cascade at sub-ion scales (Schekochihin *et al.* 2009). In this range, the two-field model simplifies and reduces, when neglecting electron inertia, to electron reduced magnetohydrodynamics (ERMHD) (Schekochihin *et al.* 2009; Boldyrev *et al.* 2013), under the conditions $\tau k_\perp^2 \gg 1$, $\tau \sim 1$,

$$\partial_t A_\parallel + \left(1 + \frac{1}{\tau}\right) \nabla_\parallel \varphi = 0 \tag{2.18}$$

$$\partial_t \varphi - \frac{\frac{2\tau}{\beta_e}}{1 + \frac{\beta_e}{2}(1+\tau)} \nabla_\parallel \Delta_\perp A_\parallel = 0. \tag{2.19}$$

In this regime, the invariants read

$$\mathcal{E} = \frac{1}{\beta_e} \int \left(|\boldsymbol{B}|^2 + \frac{2}{\beta_e} \frac{1}{1+\tau} B_z^2 \right) d^3x \tag{2.20}$$

$$\mathcal{C} = \left(1 + \frac{2}{\beta_e} \frac{1}{1+\tau}\right) \int A_\parallel B_z d^3x. \tag{2.21}$$

In the incompressible limit where the beta parameter tends to infinity, the GCH invariant reduces,in the quasi-transverse limit, to the generalized magnetic helicities of EMHD (Biskamp *et al.* 1999), or of extended MHD (XMHD) when the ion velocity and electron inertia are taken to zero (Eq. (35) of Abdelhamid *et al.* (2016) and Eq. (29) of Miloshevich *et al.* (2017)).

The magnetic field $\boldsymbol{B}$ can be written $\boldsymbol{B} = \nabla_\perp \times (A_\parallel \widehat{\boldsymbol{z}}) + B_z \widehat{\boldsymbol{z}}$. Introducing $\boldsymbol{A}_\perp$ such that $B_z = \widehat{\boldsymbol{z}} \cdot (\nabla_\perp \times \boldsymbol{A}_\perp)$, one has $\int A_\parallel B_z d^3x = (1/2) \int \boldsymbol{A} \cdot \boldsymbol{B} d^3x$ with $\boldsymbol{A} = \boldsymbol{A}_\perp + A_\parallel \widehat{\boldsymbol{z}}$ (see e.g. Eq. (F6) of Schekochihin *et al.* (2009)), together with $\int |\boldsymbol{B}|^2 d^3x = \int |\nabla_\perp \times \boldsymbol{A}|^2 d^3x$.

In the large β_e limit, $\mathcal{E} = \frac{1}{\beta_e} \int |\boldsymbol{B}|^2 dx$ and, like in incompressible MHD without ambient field (see e.g. Pouquet *et al.* (2019) for a recent review), assuming that the helicity is of a given sign and that it is maximal, one gets $E_c(k_\perp) = (1/k_\perp) E(k_\perp)$, which leads to conjecture the existence of an inverse cascade of magnetic helicity, by generalizing the argument developed by Fjørtoft (1953) for two-dimensional incompressible turbulence.

In the case of finite β_e, the energy and GCH spectra cannot be directly related to each other. Nevertheless, when turbulence is not too strong, the first and third terms in the energy given by the first line of Eq. (2.13) are approximatively in equipartition (this property was checked to be accurately satisfied in the present simulations). In the ERMHD regime, where the coefficients M_1 and M_2 are scale-independent, it is easily seen that in this case $\mathcal{E} \sim \int |\boldsymbol{B}|^2 d^3x$, which then permits using the above argument. In summary, the phenomenological argument for the existence of an inverse GCH cascade at finite β_e requires both equipartition between total magnetic and internal energies and single-sign maximal helicity, while in the large β_e limit the first condition is not necessary.

In contrast, when considering the Hall reduced magnetohydrodynamc (HRMHD) equations for dispersive Alfvén waves (Eqs. (E19)-(E20) of Schekochihin *et al.* (2009) or Eqs.(2.24)-(2.25) of Passot & Sulem (2019)), which correspond to the regime $\tau \ll 1$ and $\tau k_\perp^2 \ll 1$, $N_e(\boldsymbol{k}) \approx -k_\perp^2 \varphi(\boldsymbol{k})$ and $B_z(\boldsymbol{k}) \approx (1 + 2/\beta_e)^{-1} k_\perp^2 \varphi(\boldsymbol{k})$, one has

$$\mathcal{E} = \frac{1}{2} \int \left[\frac{2}{\beta_e} |\nabla_\perp A_\parallel|^2 + \left(1 + \frac{k_\perp^2}{1 + \frac{\beta_e}{2}}\right) \left(1 + \frac{2}{\beta_e}\right)^2 \frac{1}{k_\perp^2} B_z^2 \right] d^3x \tag{2.22}$$

$$\mathcal{C} = \left(1 + \frac{2}{\beta_e}\right) \int A_\parallel B_z d^3x = \frac{1}{2}\left(1 + \frac{2}{\beta_e}\right) \int \boldsymbol{A} \cdot \boldsymbol{B} d^3x. \tag{2.23}$$

Two regimes are then to be distinguished. When formally taking the limit $k_\perp \to \infty$ (which in the HRMHD model requires en extremely small value of τ) and assuming equipartition of the magnetic and internal energies, one writes the total energy in the form

$$\mathcal{E} = \frac{1}{\beta_e} \int |\boldsymbol{B}_\perp|^2 d^3x = \left(\frac{1 + \frac{2}{\beta_e}}{2 + \frac{2}{\beta_e}}\right) \frac{2}{\beta_e} \int |\boldsymbol{B}|^2 d^3x. \tag{2.24}$$

The same argument as in the case of ERMHD can then be used to conjecture the existence of an inverse GCH cascade. As expected, this argument does not apply in the RMHD regime corresponding to the limit $k_\perp \to 0$. Using in this case the strongest assumption of local-in-scale energy balance, one gets

$$B_z(\boldsymbol{k}) = \sqrt{\frac{2}{\beta_e}} \frac{1}{1 + \frac{2}{\beta_e}} k_\perp |\boldsymbol{B}_\perp(\boldsymbol{k})|, \tag{2.25}$$

and thus

$$\mathcal{C} = \sqrt{\frac{2}{\beta_e}} \int |\boldsymbol{B}_\perp|^2 d^3x. \tag{2.26}$$

In this case, $\mathcal{E}$ and $\mathcal{C}$ are proportional and no energetic condition prevents the existence of a simultaneous direct cascade of the two invariants. From the above argument, we can expect that an inverse cascade of GCH develops when turbulence is driven at sub-ion scales and that this cascade progressively slows down when approaching the non-dispersive scales.

3. Numerical setup and conditions of the simulations

We performed three-dimensional numerical simulations of the two-field gyrofluid, in the form given by Eq. (2.15), supplemented with injection at a wavenumber k_f and small-scale dissipation. Usually, when retaining electron inertia in Eqs (2.1)-(2.2), β_e must be small enough in order for electron FLR terms to be negligible compared to electron inertia. In order for both electron FLRs and inertia terms to be negligible at the forcing wavenumber (we here concentrate on the inverse cascade), one needs to have (in dimensional units) both $k_f \rho_e = 2^{1/2} \delta(k_f \rho_s) \ll 1$ and $k_f d_e = (2/\beta_e)^{1/2} \delta(k_f \rho_s) \ll 1$. In all the simulations listed in Table 1 (except the one with $k_f \rho_s = 36$), one has $k_f \rho_e < 1$. Electron inertia will thus be even smaller if $\beta_e \gtrsim 2$. In order to make the effects associated with electron inertia completely negligible at all the scales, we prescribed an electron-to-proton mass ratio δ^2 smaller than the physical one †.

The integration domain is assumed to be periodic of size L in the three directions, and a Fourier pseudo-spectral method was used, with aliasing suppressed by spectral truncation at 2/3 of the maximal wavenumber. Time stepping was performed using a third-order Runge-Kutta scheme. The prescribed parameters of the simulations presented in the following are described in Table 1, together with the typical level $B_\perp(k_f)$ at the injection wavenumber and a phenomenological estimate χ_f^t of the nonlinear parameter (defined below). They involve resolutions of $N = 240$ or $N = 360$ grid points in each direction and a time step Δt that has usually to be reduced as the simulation proceeds.

† After the paper has been submitted, a new version of the code integrating Eqs. (2.1) and (2.2) with $\delta = 0$ has been developed and it was checked that, for the presented simulations, the results are indeed indistinguishable.

	β_e	k_f	ϵ_E	ϵ_E/ϵ_C	$L/2\pi$	N	ν	δ^2	$\min(\Delta t)$	χ_f^t	$\lvert B_\perp(k_f)\rvert$
$R_{1.3}^{0.5}$	0.2	1.3	0.37	30.1	27.5	360	7.8×10^{-5}	10^{-5}	8.0×10^{-3}	0.17	0.40
$R_{1.3b}^{0.2}$	0.2	1.3	0.37	∞	27.5	360	7.8×10^{-5}	10^{-5}	1.0×10^{-2}	0.17	0.38
$R_{1.3sb}^{0.2}$	0.2	1.3	5.95	∞	27.5	360	7.8×10^{-5}	10^{-5}	1.0×10^{-2}	0.43	0.70
$R_{1.3}^{2}$	2	1.3	0.37	6.34	27.5	360	7.8×10^{-5}	10^{-5}	1.0×10^{-2}	0.61	1.0
$R_{1.3b}^{2}$	2	1.3	0.37	∞	27.5	360	7.8×10^{-5}	10^{-5}	1.0×10^{-2}	0.61	0.85
$R_{6.5}^{2}$	2	6.5	0.37	27.2	5.5	240	4.0×10^{-8}	10^{-6}	4.0×10^{-3}	0.22	0.27
R_{13}^{2}	2	13	0.37	54.2	2.75	240	2.5×10^{-11}	10^{-6}	5.0×10^{-4}	0.14	0.25
R_{13s}^{2}	2	13	95.2	54.2	2.75	240	1.0×10^{-10}	10^{-6}	5.0×10^{-4}	0.88	1.65
R_{13w}^{2}	2	13	0.0058	54.2	2.75	240	2.5×10^{-11}	10^{-6}	5.0×10^{-4}	0.035	0.085
R_{13b}^{2}	2	13	0.37	∞	2.75	240	2.5×10^{-11}	10^{-6}	5.0×10^{-4}	0.14	0.26
R_{13sb}^{2}	2	13	95.2	∞	2.75	240	1.0×10^{-10}	10^{-6}	5.0×10^{-4}	0.88	1.68
R_{36}^{2}	2	36.0	0.37	149	1.0	240	5.0×10^{-14}	10^{-6}	5.0×10^{-4}	0.071	0.14
R_{36b}^{2}	2	36.0	0.37	∞	1.0	240	5.0×10^{-14}	10^{-6}	5.0×10^{-4}	0.071	0.16
$R_{0.89}^{10}$	10	0.89	0.37	2.05	20.3	360	1.0×10^{-5}	10^{-5}	4.0×10^{-3}	1.74	2.3
$R_{1.3}^{10}$	10	1.3	0.37	1.94	13.5	360	4.0×10^{-7}	10^{-5}	3.125×10^{-3}	1.55	3.5
R_{2}^{10}	10	2.0	0.37	2.20	9.05	360	1.5×10^{-8}	10^{-5}	2.0×10^{-3}	1.29	2.6
$R_{6.5}^{10}$	10	6.5	0.37	6.34	5.5	240	4.0×10^{-8}	10^{-6}	2.0×10^{-2}	0.61	0.50
R_{13}^{10}	10	13	0.37	12.6	2.75	240	2.5×10^{-11}	10^{-6}	5.0×10^{-4}	0.39	0.58
R_{13}^{50}	50	13	0.37	2.63	2.75	240	2.5×10^{-11}	10^{-6}	5.0×10^{-4}	1.11	1.45
R_{36}^{50}	50	36	0.37	7.21	1.0	240	5.0×10^{-14}	10^{-6}	5.0×10^{-4}	0.57	1.1

Table 1: Parameters of the runs, together with the nonlinear parameter χ_f^t at the driving scale. Runs are named after the perpendicular wavenumber of the driving and the value of β_e, appearing respectively as subscript and superscript. Additional subscripts s and w refer to energy injection rates respectively stronger or weaker than the usual value $\epsilon_E = 0.372$. In all the simulations, $\epsilon_{E^+}/\epsilon_{E^-} = 1.5$, except in runs $R_{1.3b}^{0.2}$, $R_{1.3sb}^{0.2}$, $R_{1.3b}^{2}$, R_{13b}^{2} and R_{13sb}^{2}, where $\epsilon_{E^+}/\epsilon_{E^-} = 1$ (balanced driving).

All the simulations are driven by an additive random forcing, white-noise in time in such a way that the energy injection rate $\epsilon_E^{\pm}$ of each type of counter-propagating waves is prescribed. This is done by a forcing terms in the equations for $\widehat{D\mu^{\pm}}$, in the form of $f_{\boldsymbol{k}}^{\pm} = \frac{1}{\sqrt{\Delta t}} A^{\pm} \exp\left[-\frac{(k_\parallel - k_{0\parallel})^2}{\sigma_{0\parallel}^2}\right] \exp\left[-\frac{(k_\perp - k_{0\perp}^2)}{\sigma_{0\perp}^2}\right]$, truncated so that only wavenumbers $k_\perp$ and $k_\parallel$ such that $|k_{\parallel,\perp} - k_{0\parallel,\perp}| \leqslant 3\sigma_{0\parallel,\perp}$ are driven (in practice, only 3 Fourier modes are forced in each direction) and multiplied by a factor $a + ib$ where a and b are Gaussian real random variables of zero mean value and variance unity, drawn independently for each of the fields at each time step. In Eqs. (2.15) for $G^{\pm}$ that are integrated numerically in the following sections, this corresponds to driving terms of the form $\frac{1}{2}\left[\frac{L_e}{s} \mp \delta M_2 \Lambda^{-1}\right] D_e^{-1} f^{+} - \frac{1}{2}\left[\frac{L_e}{s} \pm \delta M_2 \Lambda^{-1}\right] D_e^{-1} f^{-}$. In addition, dissipation terms $\nu(-\Delta)^4 G^{\pm}$ are included.

When not otherwise specified, we choose $k_{0\parallel} = k_{0_\perp} = k_f$ and $\sigma_{0\parallel} = \sigma_{0\perp} = \sigma_f$. Due to the ordering underlying the derivation of the gyrofluid model (where longitudinal gradient balances transverse nonlinearity), this choice corresponds to a quasi-transverse driving in the primitive physical variables. The energy injection rate, $\epsilon_E \equiv \epsilon_E^{+} + \epsilon_E^{-}$, is chosen to be equal to 0.372 for most of the runs, while the GCH injection rate $\epsilon_C \approx (\epsilon_E^{+} - \epsilon_E^{-})/v_{ph}(k_f)$ varies with k_f and β_e. Since the goal of the simulations was to study the large-scale dynamics and because of constraints on computational resources we had to introduce hyperviscosity coefficients ν that often do not permit the development of a small-scale inertial range. As a consequence there is no real scale separation between injections and dissipation.

4. Global properties of the GCH inverse cascade

In the small-scale limit, the model reduces to ERMHD. When $\beta_e \to \infty$, this latter model can be derived in the strong anisotropic limit from EMHD (see e.g. Galtier & Meyrand (2015)) for which direct numerical simulations in the case of imbalanced driving display an inverse cascade of magnetic helicity (Kim & Cho 2015). Therefore, it is of interest to study the dynamics when the driving takes place at scales comparable to or moderately smaller than the sonic Larmor radius (taken as the length unit), for finite values of β_e.

It is first useful to define the various spectra and fluxes that will be used to illustrate the cascade properties. We denote by $E(k_\perp)$ and $E_C(k_\perp)$ (hereafter, transverse spectra) the spectral density in the transverse plane of the energy and GCH, respectively. Similar quantities $E(k_\parallel)$ and $E_C(k_\parallel)$ are defined for the parallel spectra†. Integration of these spectra with respect to the transverse ($k_\perp$) or parallel ($k_\parallel$) wavenumbers, reproduces the corresponding ideal quadratic invariants. It is also of interest to consider the Elsasser energy and GCH transverse spectra $E^{\pm}(k_\perp)$ and $E_C^{\pm}(k_\perp)$ related to the energy and GCH by the relations $E(k_\perp) = \frac{1}{2}(E^{+}(k_\perp) + E^{-}(k_\perp))$ and $E_C(k_\perp) = \frac{1}{2}(E_C^{+}(k_\perp) - E_C^{-}(k_\perp))$ with $E_C^{\pm}(k_\perp) = E^{\pm}(k_\perp)/v_{ph}(k_\perp)$. Here, $E^{\pm}(k_\perp)$ can be viewed as the spectrum of the

† Note that the parallel spectra here refer to spectra along the direction of the ambient magnetic field. Especially when the nonlinearity parameter of the simulation is of order unity, these quantities can differ from the parallel spectra associated with second-order structure functions tied to the local magnetic field lines, whose definition requires the reintroduction of a large but finite value of the ambient magnetic field (see e.g. Maron & Goldreich (2001) in the MHD case). In this case, a given field line can indeed wander throughout the whole perpendicular domain as it extends along the parallel direction, even when the field line distortion is small. This could potentially affect the interpretation of the parallel spectra of Fig. 9.

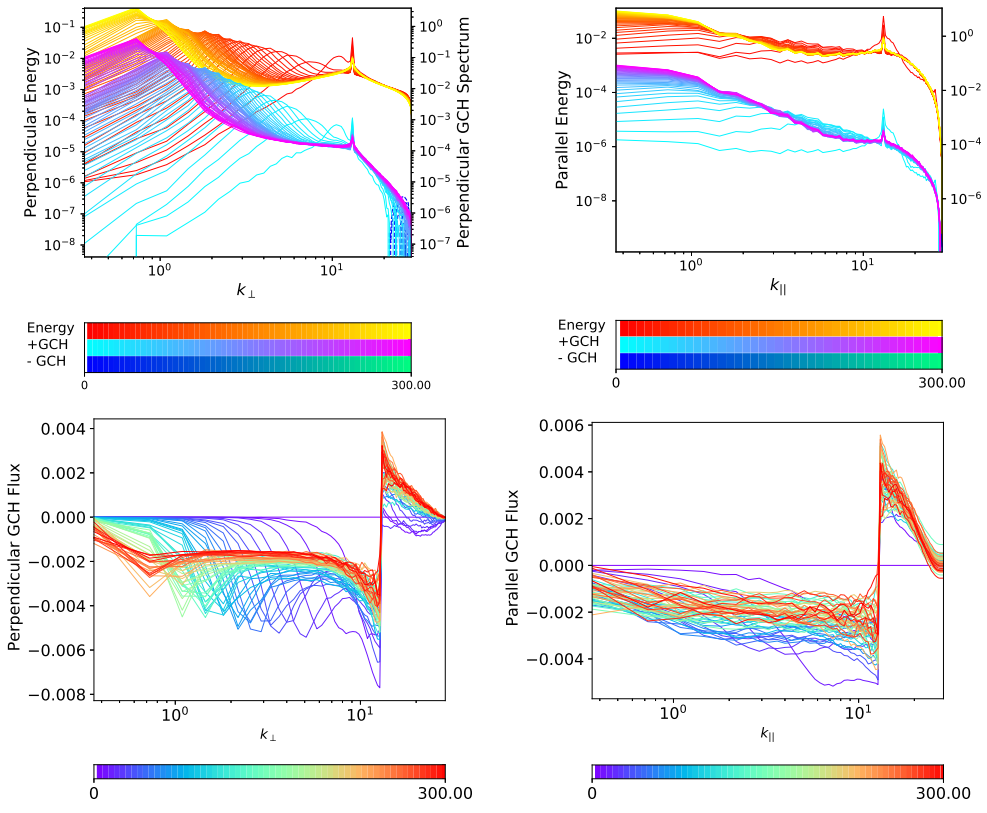


Figure 2: Perpendicular (left) and parallel (right) energy and GCH spectra (top) and GCH fluxes (bottom) for Run R_{13}^2. The integration time that extends up to $t = 300$ (in Ω_i^{-1} units) is indicated in the the color bars, where +GCH refers to positive value and -GCH to the modulus of negative values (dashed lines visible at the smallest scales) of the GCH spectra. For clarity, the axes of the energy and GCH spectra have been shifted. Same convention on forthcoming graphs.

field $D_e\mu^\pm$ and $E_C^\pm(k_\perp)$ of the field $V_{ph}^{-1/2}D_e\mu^\pm$. Furthermore, the perpendicular and parallel fluxes of the energy and GCH are respectively defined as the negative nonlinear contributions to $\partial_t \int_0^{k_\perp} E(k'_\perp)dk'_\perp$ or $\partial_t \int_0^{k_\perp} E_C(k'_\perp)dk'_\perp$(for the perpendicular fluxes) or to $\partial_t \int_0^{k_\parallel} E(k'_\parallel)dk'_\parallel$ or $\partial_t \int_0^{k_\parallel} E_C(k'_\parallel)dk'_\parallel$ (for the parallel fluxes). They are explicitly calculated using Eq. (B 1) together with Eqs. (B 20)-(B 21) of Appendix B.

After presenting our fiducial run, which will serve to illustrate the existence and main properties of the GCH inverse cascade, we will address the effect of a variation of the energy injection rate ϵ_E, and thus of the turbulence strength.

4.1. *Spectra and fluxes*

When choosing $\beta_e = 2$ and $k_f = 13$, an inverse cascade of GCH quickly develops, giving rise to a spectral bump propagating towards large transverse scales. This is illustrated in Fig. 2 (top, left). In this case, the inverse cascade extends over more than one decade before reaching the weakly dispersive scales. The observed dynamics is qualitatively similar to that obtained in numerical simulations of EMHD (Kim & Cho 2015) and

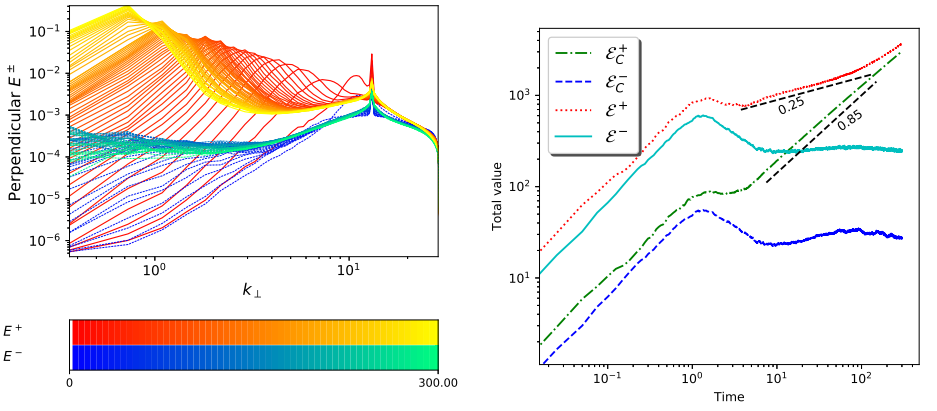


Figure 3: Perpendicular Elsasser spectra (left) and time evolution of the total Elsasser energies $\mathcal{E}^{\pm}$ and GCHs $\mathcal{E}_C^{\pm}$ (right) for Run R_{13}^2.

also of incompressible MHD in the absence of an ambient field (Müller *et al.* 2012; Linkmann & Dallas 2017). At the final time of the simulation, the energy has almost reached the lowest modes and a separate simulation is needed to address the situation where the cascade crosses $k_\perp = 1$ and penetrates into the weakly dispersive range. It will be discussed in Section 6 with run $R_{1.3}^2$.

The perpendicular GCH flux displayed in the bottom left panel shows at late times a remarkably constant range, associated with an inverse cascade, in the spectral region between the peak and the forcing. Interestingly, a self-similar inverse cascade develops in the parallel direction as well, as shown in Fig. 2 (top, right), also associated with a negative and constant GCH flux (bottom, right). The existence of this parallel inverse cascade has important consequences on the types of structures that form in physical space, as discussed in Section 8. When considering energy fluxes (not shown), we note that the perpendicular one is significant at wavenumbers larger than k_f but very small for $k_\perp < k_f$. Energy is transferred to large scales together with the cross-helicity, but only the latter undergoes a true inverse cascade. In the parallel direction, the energy flux, although not displaying a constant range, is decaying more slowly as $k_\perp$ decreases away from k_f.

In Fig. 3, we show the Elsasser spectra $E^{\pm}(k_\perp)$ (left) and the time evolution of the total Elsasser energies $\mathcal{E}^{\pm} = \sum_{k_\perp} E^{\pm}(k_\perp)$ and of the positive/negative GCHs $\mathcal{E}_C^{\pm} = \sum_{k_\perp} E_C^{\pm}(k_\perp)$ (right). The inverse GCH cascade is only associated with an inverse transfer of E^+. This behaviour is specific to cases where the ratio ϵ^+/ϵ^- is small or moderate, as also seen in EMHD simulations by Kim & Cho (2015). In this run, a non-negligible transfer of E^- is nevertheless visible, which might develop into a different type of inverse cascade involving longer spatial and temporal scales. Simulations with a spectral range extending to much larger scales and spanning a longer time interval would be necessary to characterize this effect more precisely. Both $\mathcal{E}^+$ and $\mathcal{E}_C^+$ grow at long time as power laws with exponents similar but not identical to those reported in Kim & Cho (2015) in the case of EMHD. Furthermore, we verified that, while keeping the parameters of run R_{13}^2, but injecting only one type of wave (infinitely imbalanced driving), the other type of wave is generated by interactions of driven modes. While the energy of the dominant mode is transferred to the large scales through the propagation of a spectral bump whose envelope

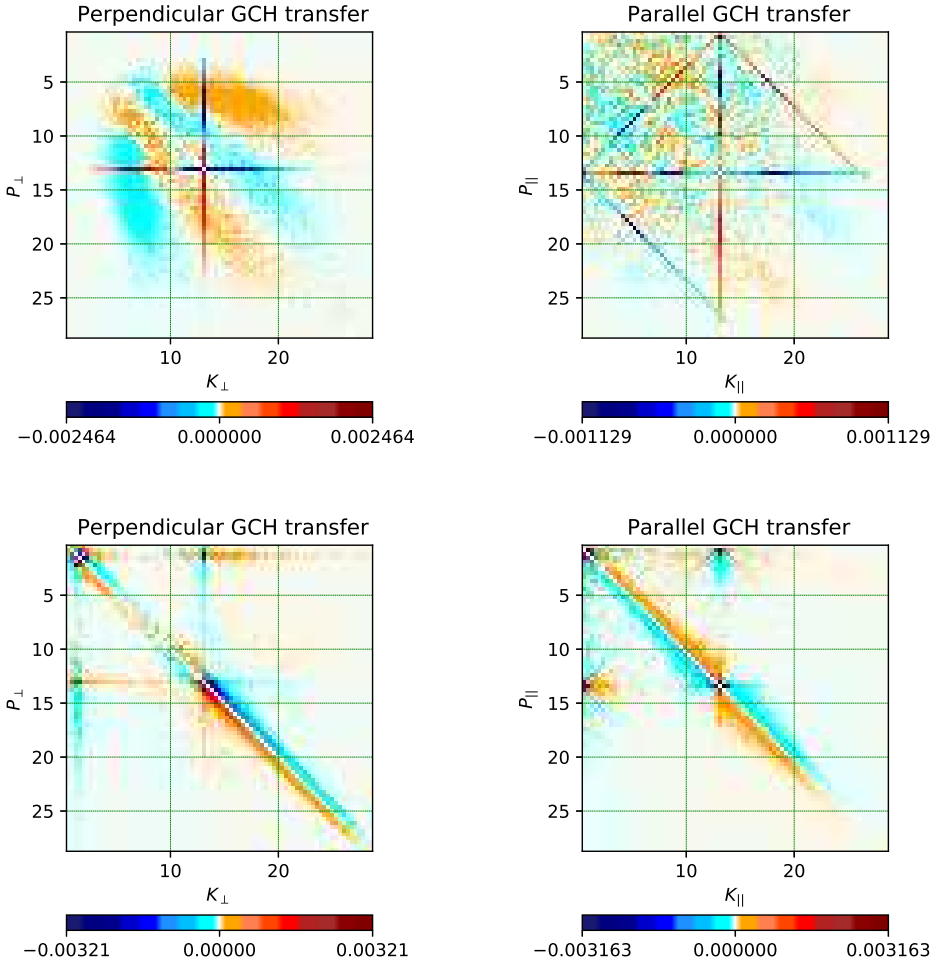


Figure 4: Perpendicular (left) and parallel (right) transfers of GCH for run R^2_{13} at an early ($t = 5$, top) or late ($t = 100$, bottom) time of the simulation.

obeys a $k_\perp^{-3/2}$ scaling law, the subdominant wave undergoes a self-similar cascade with a $k_\perp^{-1}$ spectrum (not shown), indicating a behavior of both spectra similar to that observed in EMHD simulations with maximal helicity injection (Kim & Cho 2015).

4.2. *Shell-to-shell transfers*

In the following, we analyze the shell-to-shell transfers, i.e. the amount of energy and GCH transferred per unit time from one spectral shell in the transverse plane to another, after integration on the parallel wavenumbers. The transfer between parallel wavenumbers, after integration on the transverse wavenumbers is also considered. These quantities provide useful information concerning the degree of (spectral) locality of the nonlinear interactions. Their expressions are derived in Appendix B and explicitly given in Eqs. (B 20) and (B 21). It is to be noted that in this context R^2_{13} is generic and the statements about the non-local nature of transfers apply to the other simulations. However, as shown in the following subsection, other features may differ.

Figure 4 shows the GCH shell-to-shell transfers both in the transverse plane (left) and in the longitudinal direction (right), at an early time ($t = 5$, top), and at a time close to the end of the simulation ($t = 100$, bottom). Transfers in the perpendicular directions are computed from Eqs. (B 20) and (B 21) of Appendix B. Similar expressions are used for the longitudinal transfers, where cylindrical shells are replaced by slabs.

At early time, inverse transfers of GCH appear to be strongly nonlocal, i.e. off-diagonal which indicates transfer between non-neighboring shells. We observe the characteristic cross-signature which demonstrates the interactions of the forcing with other shells. The modes located on the upper vertical and left horizontal axes that meet at the forcing wavenumber are associated with an inverse transfer close to the forcing. On the contrary, the nonlocal transfers between the forcing and the wavenumbers that are much larger, are consistently associated with direct transfers.

The inverse GCH cascade is mainly driven by the nonlocal interactions between the forcing and the propagating bump, that can be seen as the orange (cyan) areas located in the regions where $k_\perp$ (respectively $p_\perp$) is slightly smaller and larger than k_f with $p_\perp$ (respectively $k_\perp$) between 5 and 10.

In the parallel direction, there is no significant inverse transfer but interacting triads involving the forcing and its first harmonic are clearly visible (see also the parallel spectrum at the first output in the top right panel of Fig. 2). The oblique lines ($k_\parallel + p_\parallel = k_f$ and circular permutations) and those parallel to the axes ($k_\parallel = k_f$ or $p_\parallel = k_f$) correspond to the interactions between triads including the driving mode. No other interaction is significant at this early time.

The transfers at late times display more local features, both in the parallel and perpendicular directions. The perpendicular inverse transfer of GCH still involves nonlocal interactions between the spectral bump and the forcing, while energy (not shown) has predominantly local features. It is noteworthy to mention that early bump propagation is always dominated by the nonlocal cross-type interaction between the forcing and the bump. The parallel GCH transfers associated to the direct cascade towards scales smaller than the forcing is local, while the inverse parallel cascade involves both strongly local and non-local features.

5. Influence of the turbulence strength on the early-time dynamics

Since the dynamics involves both waves and the nonlinear dynamics of the purely perpendicular component, it is natural to investigate the impact of changing the amplitude of the perpendicular magnetic fluctuations. This is easily done by changing the injection rate ϵ_E.

5.1. *Varying the amplitude of the fluctuations*

When varying the energy injection rate, the nature of the turbulent cascade that develops at relatively early time changes significantly (see Fig. 5, left). At large amplitude, a self-similar cascade starts developing (as clearly seen in run R^2_{13s}) but the spectrum rapidly distorts. When the driving is decreased (run R^2_{13}), the dynamics is that of a propagating spectral bump, as described in the previous subsection. Further decreasing the injection rate, the early dynamics is dominated by the development of a parametric decay instability of the pump waves driven by the random forcing (conspicuous in Fig. 5 (left) where two bumps emerge at time $t \approx 110$). Indeed, in contrast with Alfvén waves in ideal MHD, three KAWs can interact resonantly, producing a decay instability (Voitenko 1998*a*) (see Appendix A for a brief description of this linear instability in the context of the two-field model, in the absence of injection and dissipation). This instability is

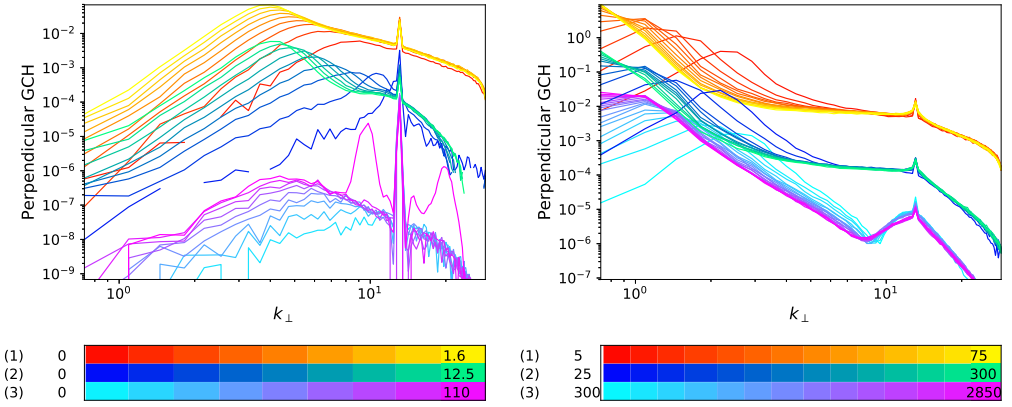


Figure 5: Snapshots at short (left) and long (right) times of the GCH spectra for runs R^2_{13s} (1), R^2_{13} (2) and R^2_{13w} (3) corresponding to strong, intermediate and weak injection rates respectively. Final times displayed in the left panel are $t = 1.6$ (1), $t = 12.5$ (2), $t = 110$ (3), and in the right panel $t = 15$ (1), $t = 300$ (2), $t = 2850$ (3).

competing with the turbulence dynamics (see Shi *et al.* (2017); Fu *et al.* (2018) for a study in the MHD context). Even though the growth rate becomes larger when the level of the magnetic fluctuations is increased, the transfer to neighboring modes due to turbulence is more efficient, thus hiding or preventing the instability. When ϵ_E is small enough, as it is the case for run R^2_{13w}, the growth rate is smaller, but the turbulence is also less efficient, making the appearance of the decay possible. A more detailed study of the resonance conditions will be discussed in the next subsection.

Decreasing ϵ_E only affects the early-time dynamics. Indeed, as seen in the right panel of Fig. 5, the late evolution of the two runs with strong and intermediate driving displays similar features associated with a strongly bent spectrum with a bump at large scale, separated from the forcing by a spectral domain where the dynamics tends to settle to an absolute equilibrium†. The case of a weak driving has the same tendency but the evolution is much slower. Similar simulations that display decay at early time but with a larger value of χ_f show in a more conspicuous way an evolution towards a flat spectrum in the range between the driving and the maximum of the spectrum.

Even if the inverse cascades displayed by the simulations previously discussed may suggest the existence of qualitatively different kinds of cascades, a more likely scenario is that there is a continuous transition between a self-similar cascade and a spectral bump propagating to large scales. Inspection of the time evolution of individual energy and GCH transverse Fourier modes indicates that when the inverse cascade reaches a given wavenumber, the corresponding modes first grow and then decrease with a characteristic decay time that becomes shorter when wave effects are enhanced. The relative effect of the strength of the turbulence compared to that of the waves, measured by the nonlinearity parameter at the driving scale χ_f, is then likely to characterize the cascade properties.

The nonlinear parameter $\chi(\boldsymbol{k})$ at the wavenumber $\boldsymbol{k}$ can be estimated as follows. From Eq.(2.2) with $\delta = 0$, we estimate the non-linear time $\tau_{NL}(k_\perp)$ (defining $\widehat{M}_3 = 1 - \widehat{M}_1 + \widehat{M}_2$)

† We indeed observe that the GCH flux (which is flat in the spectral range between the driving and the spectral bump) slowly decreases as time evolves (see Fig. 2 for run R^2_{13}).

by

$$\tau_{NL}(\boldsymbol{k})^{-1} = k_\perp^2 \widehat{M}_3 |\varphi(\boldsymbol{k})|. \tag{5.1}$$

The nonlinear parameter $\chi(\boldsymbol{k}) = \tau_{NL}(\boldsymbol{k})^{-1}/(v_{ph}k_\parallel)$ reads (using Eq. (2.9)),

$$\chi(\boldsymbol{k}) = \frac{1}{s} k_\perp \widehat{M}_2^{1/2} \widehat{M}_3^{1/2} \frac{1}{k_\parallel} |\varphi(\boldsymbol{k})|. \tag{5.2}$$

At least when the nonlinearities are not too strong, one can expect equipartition of the magnetic and potential energy spectra (see e.g. Slepyan (2015) and references therein), a property which is observed to hold with a good accuracy in the most of the simulations considered in this paper (in particular, the ratio of the two spectra at k_f is typically 1 ± 0.03, the error reaching 4% at large β_e). This leads to a phenomenological estimate that near the injection scale

$$|\varphi(\boldsymbol{k})| \approx s \widehat{M}_2^{-1/2} \widehat{M}_3^{-1/2} |\boldsymbol{B}_\perp(\boldsymbol{k})|, \tag{5.3}$$

which allows one to relate the nonlinear parameter χ_f at the injection wavevector $\boldsymbol{k}_f$ (whose perpendicular and parallel components are denoted $k_{\perp f}$ and $k_{\parallel f}$) to the magnitude of magnetic fluctuations $B_\perp(k_{\perp f}) = \sqrt{k_\perp E_{B_\perp}(k_\perp)}$ (where $E_{B_\perp}(k_\perp)$ holds for the one-dimensional transverse magnetic spectrum), by

$$\chi_f = \frac{k_{\perp f}}{k_{\parallel f}} |B_\perp(k_{\perp f})|. \tag{5.4}$$

In order to have a qualitative relation between the level of magnetic field fluctuation $|B_\perp(k_{\perp f})|$ at the driving wavenumber and ϵ_E, it is nevertheless possible to use a simple strong-turbulence phenomenology and write, still assuming energy equipartition,

$$\epsilon_E \approx \frac{2}{\beta_e} |B_\perp(k_{\perp f})|^2 \tau_{NL}(k_{\perp f})^{-1} \approx \frac{2}{\beta_e} |B_\perp(k_{\perp f})|^3 k_{\perp f} v_{ph}(k_{\perp f}). \tag{5.5}$$

This prompts the definition of the nonlinearity parameter based on turbulent phenomenology by, up to a numerical constant,

$$\chi_f^t = \frac{k_{\perp f}}{k_{\parallel f}} \left(\frac{\beta_e}{2} \frac{\epsilon_E}{k_{\perp f} v_{ph}(k_{\perp f})} \right)^{1/3}. \tag{5.6}$$

Assuming that τ is of order unity, we find, using Table 1 in Passot & Sulem (2019), that at large scales $v_{ph} \sim s$, and at small scales $v_{ph} \sim s k_\perp$ when $\beta_e \lesssim 1$ and $v_{ph} \sim s^2 k_\perp$ when β_e is large. For a driving acting at sub-ion scales, $\chi_f^t \sim \epsilon_E^{1/3} k_{\perp f}^{1/3} k_{\parallel f}^{-1} \beta_e^{1/2}$ for small or moderate β_e and $\chi_f^t \sim \epsilon_E^{1/3} k_{\perp f}^{1/3} k_{\parallel f}^{-1} \beta_e^{2/3}$ for large β_e.

The expression of the χ_f parameter suggests that the dynamics will be sensitive to the angle of the injected KAWs with respect to the ambient magnetic field. Indeed, in simulations for which $k_{\parallel f} \ll k_{\perp f}$, which makes χ_f very large, the dynamics is quasi-2D. The waves have very long time scales and the inverse cascade is more self-similar. Moreover, in these conditions, the dynamics is influenced by the quasi-conservation of the squared magnetic potential, which is observed to undergo a self-similar inverse cascade (not shown).

Note that for small β_e, where $v_{ph}\sqrt{\frac{\beta_e}{2}}$ has a finite limit, the parameter χ_f^s becomes independent of β_e when velocities are measured in units of Alfvén speed instead of sound speed and the length unit is kept unchanged. Indeed, in this limit, after a proper rescaling of the dependent and independent variables, the equations become independent of β_e and reproduce the model of Zocco & Schekochihin (2011), taken in the isothermal limit.

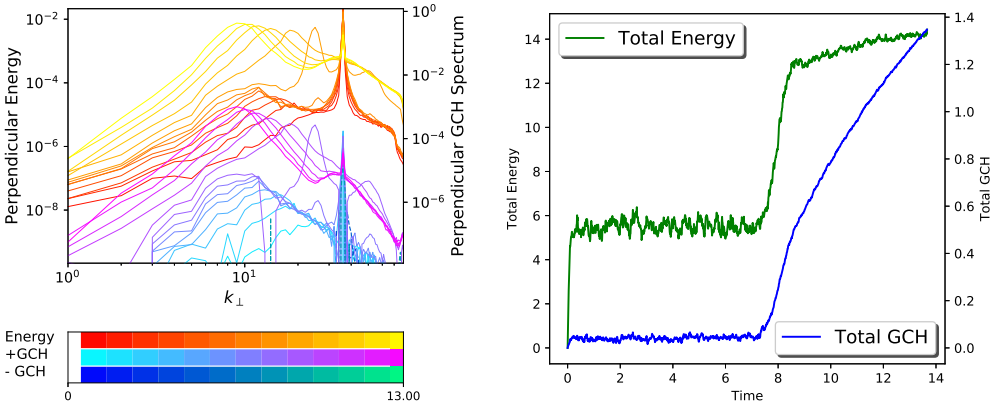


Figure 6: Transverse energy and GCH spectra (left) and time variation of the total energy and GCH (right) for run R^2_{36}.

Interestingly, the small-β_e limit is already accurately approached when $\beta_e = 0.2$. In contrast, at large β_e, the parameter χ^t_f increases with β_e, even when using the Alfvén velocity unit.

The values of χ^t_f for the different runs considered in this paper are given in Table 1, together with $|B_\perp(k_{\perp f})|$, which is measured immediately after the transient phase, at the beginning of the simulation. Note that, for some runs, $|B_\perp(k_{\perp f})|$ varies significantly during the time evolution. The ratio χ_f/χ^t_f has a mean value of 1.78 with a standard deviation of 0.43. Both quantities vary in the same way from one run to the other at moderate values of β_e, but not necessarily at larger values. Although relatively large, such uncertainty nevertheless permits using χ^t_f as a crude prediction of the nonlinear parameter χ_f which can be only measured a posteriori. It is natural to attempt to isolate the parameter χ_f to see if it solely controls the onset of self-similar - bump transitions etc. However, since it is not possible to precisely assign χ_f when initializing the simulations, we would have to initiate multiple runs to be able to select the appropriate desired values. Such ensemble would drain computational resources. Nevertheless, this conjecture that χ_f is the governing parameter appears to be consistent with the various simulations presented in this section.

5.2. *Analysis of a decay event*

Another example of the decay instability is encountered when, taking the same injection rate and β_e as for run R^2_{13}, the driving wavenumber $k_{\perp f}$ is increased to 36. Figure 6(left) clearly shows that, after the development of self-similar spectra (with exponents -2 for energy and -3 for GCH, together with a very weak negative GCH flux), a transient regime develops, corresponding to the onset of unstable modes, an effect that does not persist after turbulence has become sufficiently developed. This suggests that, if the decay instability can be a leading mechanism in the regime of weak turbulence (Voitenko 1998*b*), its effect cannot be more than a transient in the strong turbulence regime. When present, the decay instability nevertheless significantly affects the global dynamics. As seen in Fig. 6 (right), a sharp increase of the total energy and GCH takes place when the decay instability is acting. The instability can be identified at a time close to $t = 7$. Later

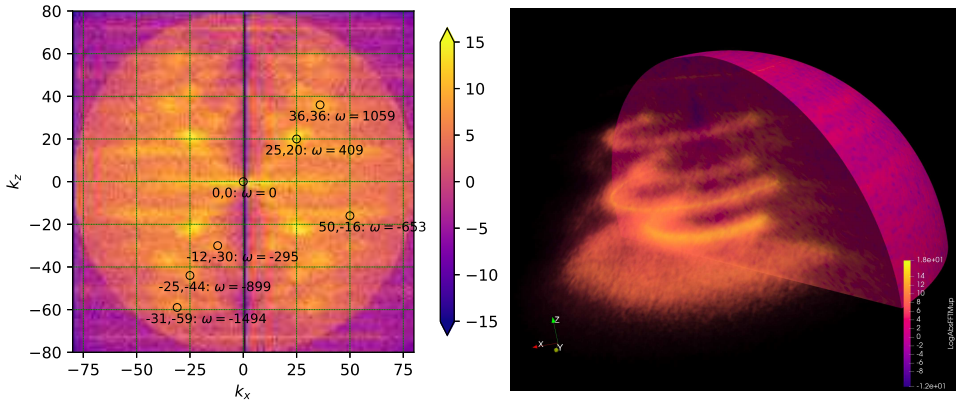


Figure 7: Color scale plot of $\ln|\widehat{\mu}^+|^2$ for run R^2_{36} showing decay instability. Left: Cross-section in a (k_x, k_z)-plane. Because the forcing is statistically isotropic in the (k_x, k_y)-plane, this plot is sufficient to characterize the full (k_x, k_y, k_z) space (see text). Among the visible peaks, some of them, such as (50,-16), (25,20) and (36,36) (which corresponds to the forcing) are associated with resonant triads. Right: Three-dimensional view. The dominant peaks visible as dots in the (k_x, k_y)-plane appear as circles symmetric around the k_z axis. Some circles are not visible since a transparency mask was applied to clearly visualize the most intensive peaks.

on, energy and GCH are still growing, but at lower rates, consistent with the existence of an inverse cascade. As expected, increasing β_e for example to $\beta_e = 50$ (not shown), the other parameters being fixed, χ_f increases to 1.1 and the decay instability is suppressed. It is also interesting to note that the cascade that develops at early time in this case is self-similar.

In order to highlight the presence of resonant interactions in run R^2_{36}, we display in Fig. 7 (left) the color scale plot of the two-dimensional spectrum $|\widehat{\mu}^+(\boldsymbol{k})|^2$ in the plane (k_x, k_z), showing decay instability at work (at $t \approx 8$). Since the forcing is statistically isotropic in the (k_x, k_y)-plane, this plot is sufficient to demonstrate the features of the full k_x, k_y and k_z dependence. We see numerous peaks, some of them associated with resonant triads. In fact, due to axisymmetry, each peak is essentially a circle penetrating the plane (see Fig. 7 (right)). This is important when evaluating the resonance condition since it provides more freedom in choosing the corresponding k_x and k_y wavevector components. Of particular interest are triads with coordinates in the (k_x, k_z)-plane given by (50,-16), (25,20) and (36,36) (which corresponds to the forcing). We indeed see that, for this triad, both $k_{1z} + k_{2z} = k_{fz}$ and $\omega_1 + \omega_2 = \omega_f$. In this context, what appears as k_x should be viewed as $k_\perp$. Resonance conditions in the transverse plane then consist of 5 equations (3 norms of transverse wavevectors and 2 resonance conditions) for 6 unknowns. Choosing arbitrarily one of them, we can easily construct a resonant triad. There is thus an infinite number of such resonant triads which can be viewed as defining a resonant manifold.

5.3. *Instability of the balanced state*

The case where the μ^+ and μ^- waves are driven in a balanced way, i.e. with a zero GCH injection rate, is illustrated with run R^2_{13b}, for which $\chi_f = 0.26$, in Fig. 8. The left panel shows the energy spectra $E^\pm$ of the two counter-propagating waves. We observe that the balanced regime is unstable. The spectra of the counter-propagating waves, which identify at early times, separate and their difference increases with time. While positive

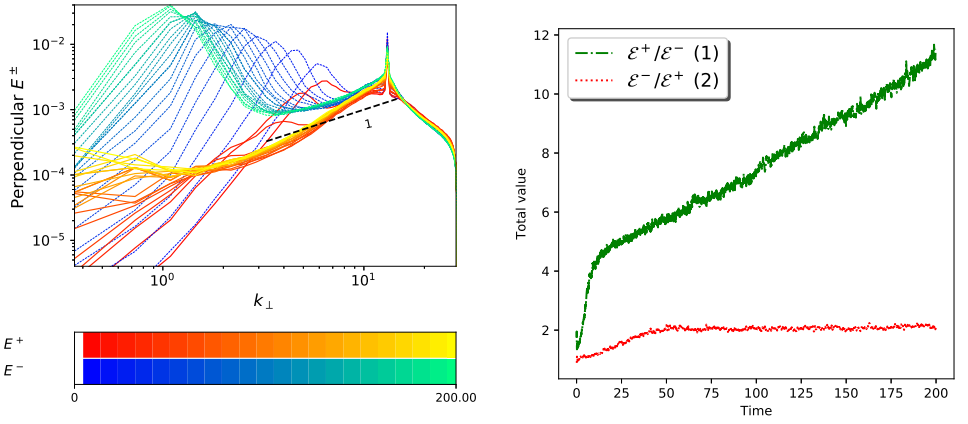


Figure 8: Left: $E^{\pm}(k_\perp)$ spectra for run R^2_{13b} resulting from a balanced driving. Right: time evolution of $\mathcal{E}^-/\mathcal{E}^+$ for run R^2_{13b} (red line) and of $\mathcal{E}^+/\mathcal{E}^-$ for run R^2_{13} (green line). The balanced state is unstable and evolves to a regime where $\mathcal{E}^-/\mathcal{E}^+ \simeq 2$.

GCH is transferred towards small scales and dissipated, negative GCH is transferred towards large scales, creating a finite global imbalance. As seen on the right panel, after some time, the global imbalance of run R^2_{13b}, as measured by the ratio $\mathcal{E}^+/\mathcal{E}^-$ of the energy of the counter-propagating waves, saturates to a value close to 0.5, in contrast with the simulation with imbalanced driving for which this ratio keeps increasing with time. Interestingly, when the energy injection rate ϵ_E is increased by a factor 256 (run R^2_{13sb}), leading to $\chi_f = 1.68$, balanced turbulence becomes stable. Another example where the balanced regime is unstable is provided by R^2_{36b} for which $\chi_f = 0.16$. In this case, we first observe a decay instability before the amplitudes of the counter propagating waves separate (not shown).

When for the same β_e, and the same energy injection rate, the wavenumber k_f is reduced to 1.3 (run $R^2_{1.3b}$), thus increasing the value of χ_f to 0.85, the instability is suppressed. It is recovered when reducing β_e to 0.2 (run $R^{0.2}_{1.3b}$), which has the effect of reducing χ_f to 0.38. When, keeping $\beta_e = 0.2$ and $k_f = 1.3$, the energy injection rate is increased by a factor 16 (run $R^{0.2}_{1.3sb}$), $\chi_f = 1.68$ and the instability is again suppressed. A more quantitative study would be required to determine a precise instability threshold and to confirm the prediction that χ_f is the only governing parameter that governs the apparition of the instability of the balanced state.

6. Inverse cascade near the weakly dispersive range

The goal of this section is to investigate the behavior of the inverse cascade as the energy bump reaches the weakly dispersive range, i.e. for $k_\perp < 1$. We thus keep $\beta_e = 2$ and the same value of ϵ_E as in run R^2_{13} but the driving is now centered at $k_f = 1.3$ (run $R^2_{1.3}$). As a result, the value of χ^t_f is larger. The top panels of Fig. 9 respectively display the transverse spectra $E(k_\perp)$ and $E_C(k_\perp)$ (left) and the parallel spectra $E(k_\parallel)$ and $E_C(k_\parallel)$ (right) at increasing times. Inspection of these spectra also indicates the existence of an inverse cascade. In contrast with run R^2_{13}, at early time both $E(k_\perp)$ and $E_C(k_\perp)$ developa self-similar range displaying a $k_\perp^{-2}$ power-law. The similarity between the $E(k_\parallel)$ and $E_C(k_\parallel)$ results from the very weak variation of the parallel phase velocity

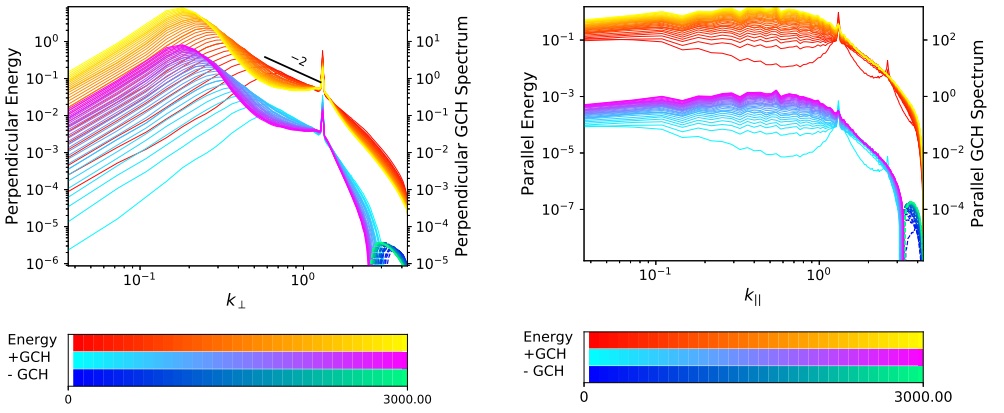


Figure 9: Perpendicular (left) and parallel (right) energy and GCH spectra for run $R^2_{1.3}$.

v_{ph} in this spectral range for $\beta_e = 2$ (see Fig. 1). This self-similar dynamics does not however proceed to longer times. After the cascade reaches scales where the variation of $v_{ph}(k_\perp)$ becomes very small, the transfer to larger scales slows down significantly while the amplitude of the spectra still increases under the effect of the persistent driving. As a result, the spectra tend to bend, flattening close to the driving wavenumber and developing a spectral bump at the minimal excited wavenumber. The slowing down is evident from the fact that the position of the spectral maximum follows two different power laws in time, behaving like $t^{-1/3}$ in the dispersive range and like $t^{-1/2}$ in the the weakly dispersive range. On the contrary, for the (clear) bump of run R^2_{13} the dependence in the dispersive range is of the form $t^{-2/3}$. Longer integrations are needed to check whether this behaviour is persistent.

Interestingly, this cascade depletion is the result of the inner turbulence dynamics, due to a strong decrease of the dispersion, with no need for an external effect such as a hypo-viscosity, as required for example in simulations of the inverse magnetic helicity cascade in incompressible isotropic MHD (Linkmann & Dallas 2017) or in EMHD (Kim & Cho 2015). In contrast, in the parallel direction, no inverse cascade is observed. Both the energy and GCH spectra become flat, corresponding to an absolute equilibrium regime where the energy is uniformly distributed among the $k_\parallel$ wavenumbers.

The existence of an inverse cascade of GCH in the transverse spectral plane is also conspicuous when considering the transverse GCH flux (not shown) which displays a flat range between the injection wavenumber and the maximum of the perpendicular spectra. Compared to R^2_{13}, in $R^2_{1.3}$ the transverse energy flux is also flat in this spectral range, but it is significantly stronger at scales smaller than the driving, suggesting a split cascade with most of the energy transferred to the small scales.

7. Impediment to the transverse cascade and formation of a finite-scale condensate

As mentioned previously, the shape of the dispersion curve has an important effect on the cascade dynamics. In order to confirm that the spectral location of this condensate corresponds to the minimum of the parallel phase velocity, we show in Fig. 10 two simulations with a driving at $k_f = 13$, where $\beta_e = 10$ (top) and $\beta_e = 50$ (bottom).

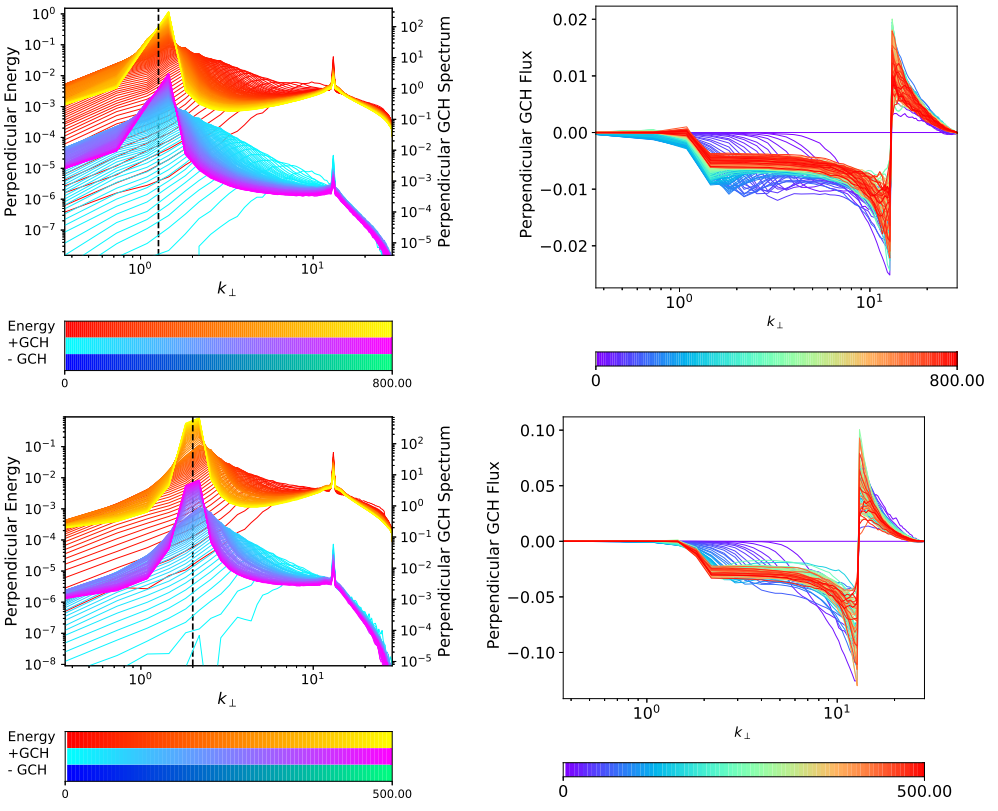


Figure 10: Energy and GCH spectra (left) and perpendicular GCH flux (right) for Run R_{13}^{10} (top) and R_{13}^{50} (bottom). In the former simulation, the maximum of the spectral bump is located at $k_\perp = 1.3$ and in the latter at $k_\perp = 2$, corresponding to the respective local minima of the parallel-phase velocity v_{ph} for the respective β_e, displayed in Fig. 1.

In the case where $\beta_e = 10$, the cascade clearly stops at a perpendicular wavenumber slightly larger than unity, where the energy and GCH accumulate at late times.

A similar behavior is observed in the left bottom panel for $\beta_e = 50$, but in this case the peak is centered at a slightly larger wavenumber, at a value close to $k_\perp = 2$. It turns out that the wavenumbers where the cascade is arrested precisely correspond to the minimum of the parallel phase velocity, as displayed in Fig. 1, and only depend on the parameter β_e. It is remarkable that such a small variation in the curvature of this quantity (e.g. between the cases $\beta_e = 2$ and $\beta_e = 10$) can lead to such an important dynamical effect.

In both cases, the arrest of the cascade leads to the development of a flat GCH spectrum, together with an energy spectrum growing like $k_\perp$, at scales slightly larger than the injection scales. Such an effect was also observed in simulations of the inverse cascade of magnetic helicity in MHD after the cascade has been arrested by the effect of an hypo-diffusivity (Linkmann & Dallas 2017). These spectra correspond to those predicted by absolute equilibrium arguments by Linkmann & Dallas (2016) (up to the geometrical factors associated with space dimension). In the case of the present model, the GCH spectrum $E_C(k_\perp)$ and the energy spectrum $E(k_\perp)$, are related, in the strongly imbalanced regime, by $E_C(k_\perp) = E(k_\perp)/v_{\rm ph}(k_\perp)$, which leads us to predict that they will have a similar slope for scales larger than the ion-scale but that $E_C(k_\perp)$ will be steeper

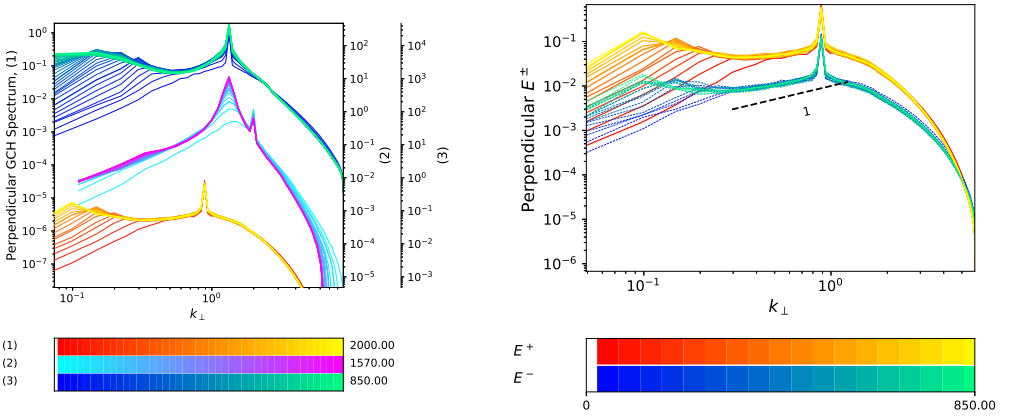


Figure 11: Left: perpendicular GCH spectra for runs $R^{10}_{0.89}$ (1), R^{10}_{2} (2) and $R^{10}_{1.3}$ (3). Right: $E^{\pm}(k_\perp)$ spectra for run $R^{10}_{0.89}$ (1).

than $E(k_\perp)$ by a factor of $k_\perp$ at sub-ion scales. Energy equipartition between the modes corresponds to transverse and parallel energy spectra scaling like $k_\perp$ and $k^0_\parallel$ respectively.

In order to highlight the sensitivity of the nonlinear dynamics to the shape of the phase velocity, we performed simulations, keeping $\beta_e = 10$, while the injection wavenumber k_f was taken slightly larger than, equal to or slightly smaller than the wavenumber $k_m = 1.3$ where v_{ph} has a minimum. The left panel of Fig. 11 displays the transverse GCH spectra corresponding to these three runs R^{10}_{2}, $R^{10}_{1.3}$ and $R^{10}_{0.89}$. For $k_f = 2$, thus larger than k_m, the cascade is arrested at this latter wavenumber. A zone of negative GCH transverse flux develops in the small spectral range between the driving and the spectral peak, which only forms on the dominant wave (not shown). In contrast, for $k_f = 1.3$ or 0.89 (thus $k_f \leqslant k_m$), a weak non self-similar inverse transfer of energy and GCH develops at large scales, with a GCH flux that is essentially zero (not shown). A tendency for analogous behavior can be inferred from the GCH spectrum of run $R^{10}_{1.3}$ (cf. the small knee in the spectrum at $k_\perp \approx 0.3$), but the dynamics is much slower than for the two other simulations. Additional information is provided by the Elsasser spectra $E^{\pm}$ of run $R^{10}_{0.89}$ displayed in the right panel. Transfer to the large scales in run $R^{10}_{0.89}$ takes place in a similar way for both waves, in contrast with the simulations presented in previous sections in which only the dominant wave cascades. This large-scale part of the cascade, which is associated with a very small negative flux (not shown) is thus of a different nature and much slower, possibly due to the negative curvature of the parallel phase velocity in this range† This point deserves a more detailed investigation in future.

8. Structures in physical space

Another point, important in the context of the formation of coherent structures, concerns the existence of a parallel inverse cascade. When comparing GCH parallel spectra of the fiducial run displayed in Fig. 2 with those of Fig. 9, it becomes evident that there is a transition from a split cascade with a significant inverse parallel component for run R^{2}_{13} at large k_f, to a predominantly forward cascade in run $R^{2}_{1.3}$ at smaller k_f.

† In the context of weak turbulence, resonant three-wave interactions are impossible for negative dispersion (i.e. negative curvature) (Zakharov *et al.* 1992) and four-wave processes then have to be taken into account.

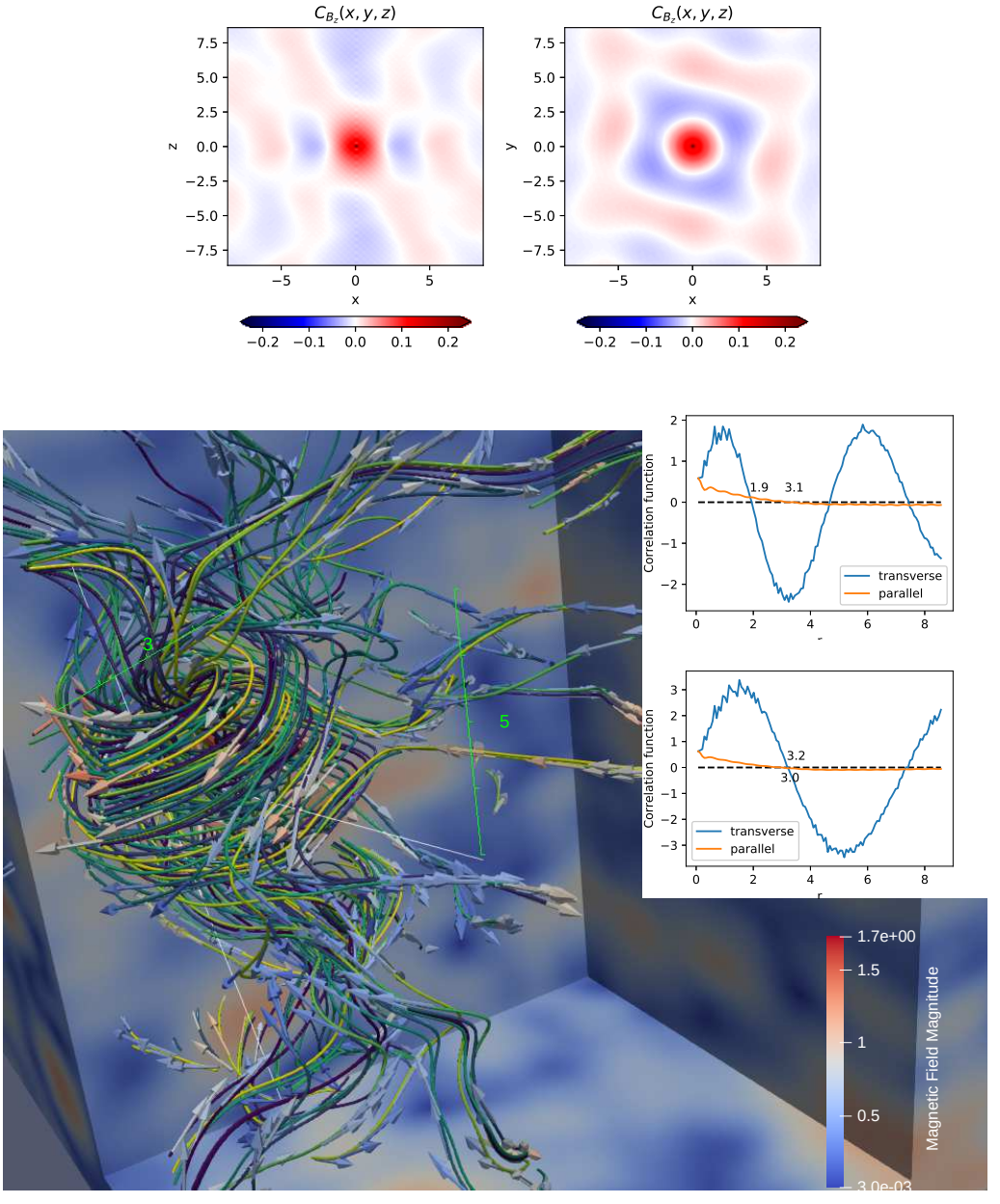


Figure 12: Top panels: The parallel and perpendicular cross-sections containing the origin of the correlation function defined in Eq. (8.1). Panels below on the right: radial (blue line) and longitudinal (orange line) dependence of the correlation function integrated over the azimuthal angle and restricted to $z = 0$ and $|\mathbf{r}_\perp| = 0$ respectively. Bottom panel: Magnetic-perturbation field lines for run R^2_{13} at an intermediate time of the simulation, showing the formation of an elongated vortex. The field has been filtered to remove the imprint of the small scales such as forcing and dissipation. Field lines are differentiated by colors. Arrows indicate the direction of the field. Color map corresponds to the magnitude of the magnetic field both on the arrows and on the horizontal and the vertical cuts. The typical size of the 3D structures is indicated using green rulers.

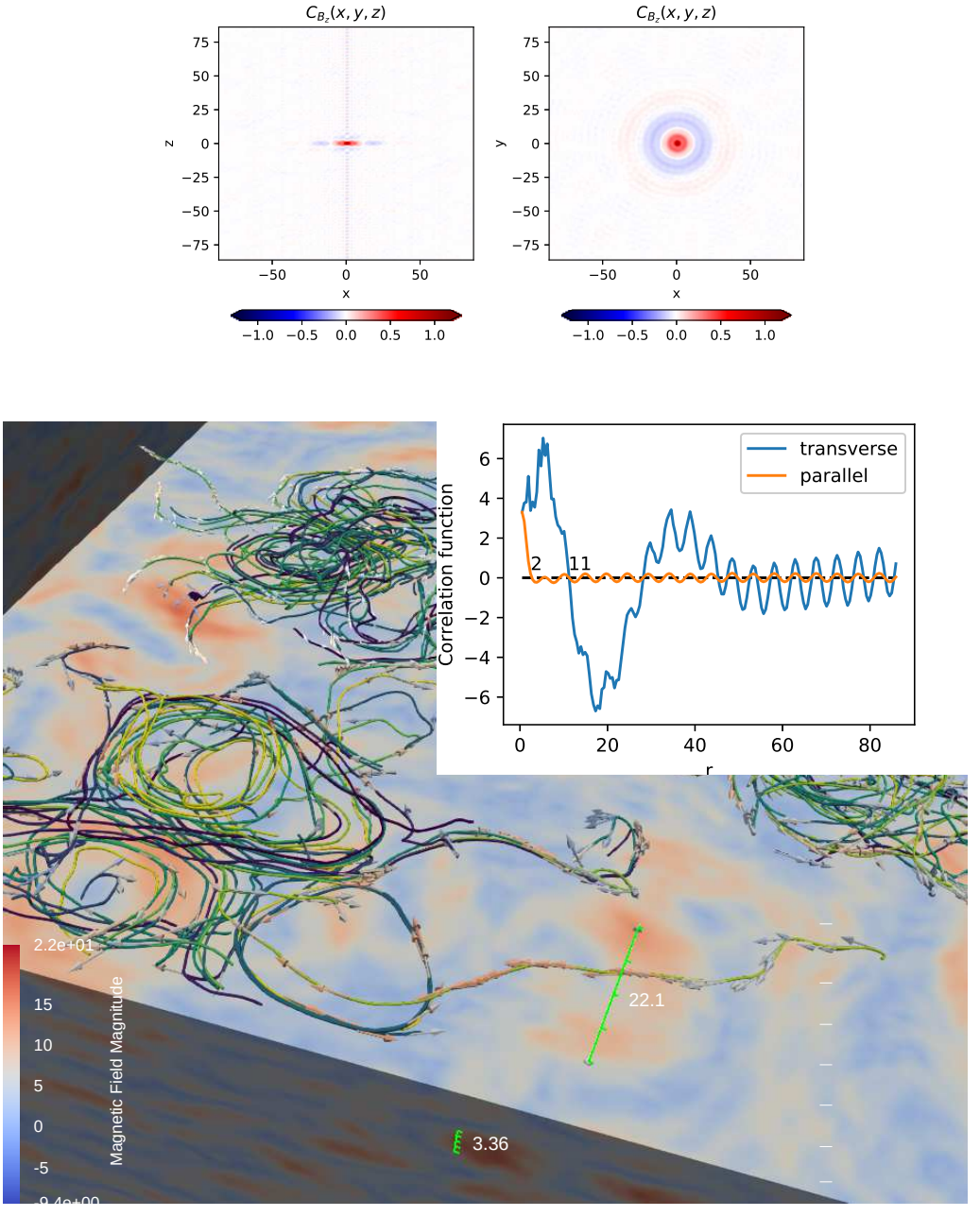


Figure 13: Top panels: vertical (left) and horizontal (right) cuts through correlation functions. Panel below on the right: radial (blue line) and longitudinal (orange line) dependence of the correlation function integrated over the azimuthal angle and restricted to $z = 0$ and $|\mathbf{r}_\perp| = 0$ respectively. Bottom panel: Magnetic-fluctuation field lines for Run $R^2_{1.3}$, showing a layer of looping filaments at a time corresponding to the late stage of the simulation. Field lines are differentiated by colors. Arrows indicate the direction of the field. Color map corresponds to the magnitude of the magnetic field both on the arrows and on the horizontal and the vertical cuts. The typical size of the 3D structures is indicated using green rulers.

In the latter case, the beating of $\pm k_z$ modes can feed the zero mode in the parallel direction and further interactions can then drive the intermediate modes to an absolute equilibrium. We checked that a parallel inverse cascade only develops when k_f is large enough. A precise determination of the condition for the existence of a parallel cascade would require a large number of simulations and is outside the scope of this paper.

These qualitative spectral features have interesting consequences in physical space. As in two-dimensional hydrodynamics, we can expect the formation of large-scale vortices, but the situation is more complex due to the three-dimensional nature of the dynamics and due to the different types of behavior in the parallel direction. To give a general overview, the transverse magnetic field appears to form various inter-connected vortices, with a typical diameter that can be appreciated from the wavenumber corresponding to the maximum in the energy or helicity spectrum. Alternatively one may estimate the size of these structures based, for example, on the behavior of the B_z-correlation function, defined as

$$C_{B_z}(\mathbf{r}) := \int d^3x \; B_z(\mathbf{x}+\mathbf{r})B_z(\mathbf{x}). \tag{8.1}$$

As the perpendicular inverse cascade proceeds, the structures, which originate from initial fluctuations at a scale comparable to the forcing, grow in time. For $\beta_e > 3.5$, this process continues until the finite-$k_\perp$ condensate is reached. For smaller β_e, no condensate forms but the dynamics slows down significantly when approaching the MHD scales. Therefore several large-scale vortices may exist simultaneously in a large enough domain, even at late times. As a representative case, consider the fiducial run that develops the vortex presented in Fig 12 (bottom panel). The field line filaments displayed in this figure are associated with the magnetic fluctuations $\boldsymbol{B} = \nabla_\perp \times (A_\parallel \widehat{\boldsymbol{z}}) + B_z \widehat{\boldsymbol{z}}$. We observe a vortex whose diameter can be roughly estimated as 3 to 4 length units, while the vertical extension are 5 to 6 units. The size estimates correspond to the domain of increased field intensity, as displayed by the color of the arrows. The parallel and perpendicular cross-sections containing the origin of the correlation function defined in Eq. (8.1) are displayed in the left and right top panels respectively. In the inserted panels, we have plotted the radial (blue line) and longitudinal (orange line) dependence of the correlation function integrated over the azimuthal angle and restricted to $z = 0$ and $|\boldsymbol{r}_\perp| = 0$ respectively. The top right inserted panel, which corresponds to the time at which the vortex is displayed, has two maxima. The typical transverse (parallel) size of the vortices corresponds to the distance at which the radial (longitudinal) correlation functions reach zero and the distance (in the transverse direction) between vortices of the same sign is given by the distance between the two maxima. The bottom right panel shows the same plots at a later time when the cascades have reached the largest scales of the domain. From these figures, we can conclude that the typical vortices that are formed have generally elongated features, with an aspect ratio of order unity (in the rescaled variables of the model). Note that when transforming the rescaled coordinates to the physical ones, the structures are to be stretched along this direction by a quantity given by the inverse expansion parameter, for example the degree of spectral anisotropy.

The parallel inverse cascade affects the parallel correlation length of the fluctuating magnetic field of vortices. In particular, in run $R^2_{1.3}$, no inverse cascade takes place in the parallel direction and, consequently, the structures in physical space are found to be flattened in horizontal layers, as shown in Fig. 13.

Figure 14 provides a schematic graphical summary of the performed simulations, together with the phenomenology observed in different regimes, in a phase diagram whose axes correspond to the driving wavenumber k_f and the electron beta parameter

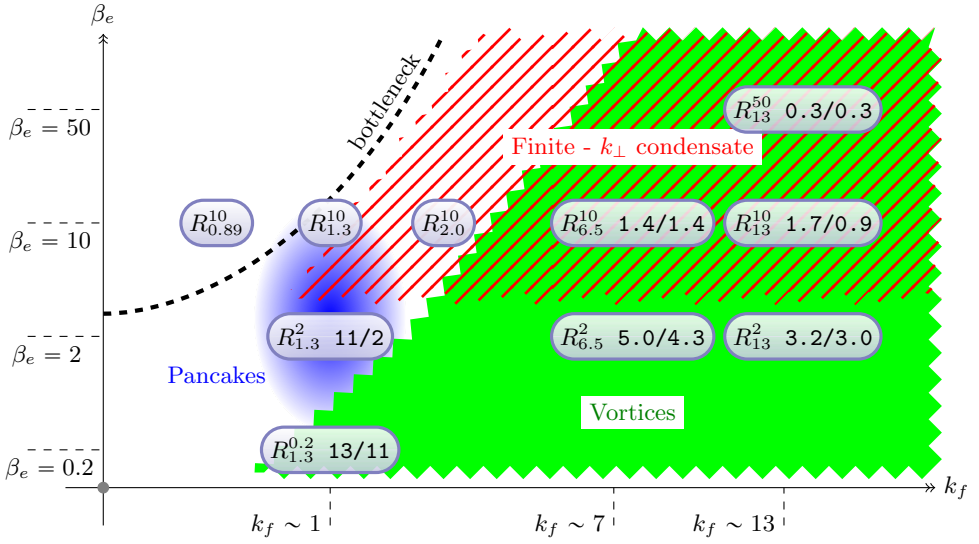


Figure 14: Phase space diagram in the (k_f, β_e)-plane, where the locations of the various types of cascades and structures in physical space are indicated as shaded areas. The relevant runs are also added in the diagram, together with the bottleneck locus associated with the values of $k_\perp$ where the parallel phase velocity has a minimum. The two numbers on the right of the run label provide the estimated correlation lengths in the transverse/parallel format.

β_e. The two additional numbers following the run labels correspond to the transverse and longitudinal correlation lengths determined using the approach described above. We can see from the figure that there are two main intersecting areas at sub-ion scales: the green part of the phase space, which corresponds to finite aspect ratio vortices, and the red part which corresponds to the runs with $\beta_e > 3.5$ that, due to the existence of a local minimum in the phase velocity curve, produce a finite-$k_\perp$ condensate. The "bottleneck" curve is the locus of points on the diagram for which v_{ph} displays such a minimum.

For moderate values of β_e, a transition is also observed close to the ion scale between situations without a parallel inverse cascade (at smaller values of k_f), where pancake structures are observed, and those at larger k_f where a clear inverse cascade develops in the parallel direction, associated with more elongated vortices. As we cross the bottleneck curve we encounter a critical behavior described in Section 7, associated with runs at $k_f \sim 1$. Beyond, for scales much larger than the ion sonic Larmor radius, the dynamics is dominated by the forward cascade of GCH, that we do not address in this paper. Below the red region, we have runs that do not produce finite-$k_\perp$ condensate, since the minimum in phase velocity disappears. It must be born in mind that only a selected choice of runs is available for drawing general conclusions, and therefore, this diagram has to be understood as a qualitative approximation.

9. Conclusion

Direct numerical simulations of a two-field gyrofluid model for KAW turbulence randomly driven at the sub-ion scales have been presented. A main observation is the development of an inverse cascade of GCH in the transverse direction and, to a lesser degree, of energy. This cascade is essentially nonlocal and some of its properties are

sensitive to the nonlinearity parameter χ_f (ratio of the period of the waves to the characteristic nonlinear time at the driving scale), and to the shape of the dispersion relation. When χ_f is large enough, a self-similar cascade develops at early time while, for smaller values of χ_f, a spectral bump is observed to propagate towards small wavenumbers. In the latter case, transient parametric decay instability events are also possible, which enhance the development of the cascade. At later times, we observe a similar evolution in all the simulations, where the spectrum gets distorted, with the establishment of an absolute equilibrium range extending from the forcing wavenumber to larger scales. When the cascade reaches non-dispersive scales, it slows down while the maxima of the energy and GCH spectra still increase. For the moderate values of the GCH injection rate we use throughout the paper, one type of wave is usually dominant, while the other develops an equilibrium spectrum. When the injection wavenumber is large or β_e small enough (i.e. when χ_f is small), an inverse GCH cascade is even possible when the driving is balanced. This result suggests that fast magnetic reconnection events could not only drive small-scale turbulence (Cerri & Califano 2017), but also induce a cascade to larger scales, a dynamics somewhat similar to the island merging proposed in Franci *et al.* (2017). When $\beta_e \gtrapprox 3.5$, the parallel-phase velocity $v_{ph} = \omega/k_\parallel$ displays a minimum at a perpendicular wavenumber close to the ion scale. In this case, the inverse GCH cascade is arrested, leading to the formation of finite-wavenumber condensates. In the parallel direction, depending on the parameters, an inverse cascade resulting mostly from local interactions can also develop.

Another result concerns the capability of the transverse GCH inverse cascade to lead to the formation of coherent vortices with a transverse size comparable to the ion scale. Depending on the plasma parameters, their longitudinal correlation length can be enhanced when an inverse cascade develops in the parallel direction. Typically, the structures that form have an aspect ratio of order unity in the anisotropic coordinates used in the model. They will be more elongated in the physical coordinates by a quantity given by the inverse expansion parameter, associated with the amplitude of the fluctuations. These structures are possibly related to those observed in the solar wind (Perrone *et al.* 2017) or in the terrestrial magnetosheath (Wang *et al.* 2019), which in some instances are associated by Alexandrova (2008) to the $k_\perp^{-4}$ transition range. The simulations we have discussed above provide a natural way to form vortices, and to demonstrate their dynamical stability. Futher development would be needed to analyze the process of their formation, i.e. whether it proceeds in a conventional two-dimensional hydrodynamics sense of vortex merger/nucleation, and if one can observe instances of reconnection, as discussed by Zhou *et al.* (2020) in the context of RMHD. Another issue is the analytical characterization of these vortices and the comparison with the Alfvén vortices found analytically in Petviashvili & Pokhotelov (1992) at MHD scales or in Jovanović *et al.* (2020) (and references therein) at ion scales and large values of the beta parameter.

The present study can be extended to include the coupling to slow magnetosonic waves, using a four-field gyrofluid model (Tassi *et al.* 2020). This description appears especially relevant in the regions near the Sun, explored by Parker Solar Probe and Solar Orbiter, where large-scale compressibility effects are important. Such a model allows for the development of the Alfvén wave parametric decay instability, an effect that is viewed as an efficient process for generating counter-propagating waves, requested for the existence of turbulence at the MHD scales (Viñas & Goldstein 1991; Del Zanna *et al.* 2001; Shoda & Yokoyama 2018).

Another avenue could involve an detailed theoretical understanding of the impediment

of the inverse cascade and the formation of a finite-$k_\perp$ condensate, observed in the simulations in the presence of a small depression in the KAW parallel-phase velocity.

Acknowledgments

This work was granted access to the HPC resources of CINES/IDRIS under the allocation A0060407042. Part of the computations have also been done on the "Mesocentre SIGAMM" machine, hosted by Observatoire de la Côte d'Azur. We are thankful to D. Borgogno for his contribution to the initial version of the numerical code.

Appendix A. Decay instability

Using the same notation for the operators and their Fourier symbols, we define the Fourier components $c_{\boldsymbol{k}}^{\sigma_k} = D_e(k_\perp)\mu_{\boldsymbol{k}}^{\sigma_k}$ of the fields $D\mu^{\pm}$ (where $\sigma_k = \pm$) and, in the interaction representation,

$$a_{\boldsymbol{k}}^{\sigma_k} = e^{i\omega_k^{\sigma_k} t} c_{\boldsymbol{k}}, \tag{A 1}$$

with $\omega_{\boldsymbol{k}}^{\sigma_k} = \sigma_k v_{ph}(k_\perp)k_z$. The gyrofluid equations rewrite

$$\partial_t a_{\boldsymbol{k}}^{\sigma_k} - \int \sum_{\sigma_p,\sigma_q} e^{i\Omega_{\boldsymbol{k};\boldsymbol{pq}}^{\sigma_k\sigma_p\sigma_q} t} V_{\boldsymbol{kpq}}^{\sigma_k\sigma_p\sigma_q} a_{\boldsymbol{p}}^{\sigma_p} a_{\boldsymbol{q}}^{\sigma_q} \delta(\boldsymbol{p}+\boldsymbol{q}-\boldsymbol{k}) d\boldsymbol{p} d\boldsymbol{q} = 0, \tag{A 2}$$

where we define

$$\Omega_{\boldsymbol{k};\boldsymbol{pq}}^{\sigma_k\sigma_p\sigma_q} = \omega_{\boldsymbol{k}}^{\sigma_k} - \omega_{\boldsymbol{p}}^{\sigma_p} - \omega_{\boldsymbol{q}}^{\sigma_q} = \sigma_k v_{ph}(k_\perp)k_\parallel - \sigma_p v_{ph}(p_\perp)p_\parallel - \sigma_q v_{ph}(q_\perp)q_\parallel.. \tag{A 3}$$

When neglecting electron inertia,

$$V_{\boldsymbol{kpq}}^{\sigma_k\sigma_p\sigma_q} = \frac{1}{8}\frac{\sigma_p\sigma_q(\widehat{\boldsymbol{z}}\cdot(\boldsymbol{p}\times\boldsymbol{q}))}{k_\perp p_\perp q_\perp}\left(\frac{\sigma_p}{\xi(p_\perp)} - \frac{\sigma_q}{\xi(q_\perp)}\right)\left(\sigma_k k_\perp^2\xi(k_\perp) + \sigma_p p_\perp^2\xi(p_\perp) + \sigma_q q_\perp^2\xi(q_\perp)\right) \tag{A 4}$$

with $\xi = s/v_{ph}$, consistent with the vertex given in Eq. (6.4) of Voitenko (1998*a*), directly derived from the Vlasov-Maxwell equations.

At this point it is easy to estimate the growth rate of the decay parametric instability of a KAW into two other KAWs. For this purpose, one considers a pump of type σ_k, with wavenumber $\boldsymbol{k}$, frequency $\omega_{\boldsymbol{k}}$ and complex amplitude $a_{\boldsymbol{k}}^{\sigma_k} = D_e\left(\Lambda\varphi(\boldsymbol{k},t) + \sigma_k A_\parallel(\boldsymbol{k},t)\right)$ (see Eq. ((2.10)). It can interact with KAWs of wavevectors $\boldsymbol{p}$ and $\boldsymbol{q}$ that satisfy the resonance conditions

$$\boldsymbol{k} = \boldsymbol{p} + \boldsymbol{q} \tag{A 5}$$

$$\omega_{\boldsymbol{k}} = \omega_{\boldsymbol{p}} + \omega_{\boldsymbol{q}}, \tag{A 6}$$

in the way that

$$\partial_t a_{\boldsymbol{p}}^{\sigma_p} = V_{\boldsymbol{p}\,\boldsymbol{k}\,-\boldsymbol{q}}^{\sigma_p\sigma_k\sigma_q} a_{\boldsymbol{k}}^{\sigma_k} a_{\boldsymbol{q}}^{\sigma_q *} \tag{A 7}$$

$$\partial_t a_{\boldsymbol{q}}^{\sigma_q *} = V_{-\boldsymbol{q}\,-\boldsymbol{k}\,\boldsymbol{p}}^{\sigma_q\sigma_k\sigma_p} a_{\boldsymbol{k}}^{\sigma_k *} a_{\boldsymbol{p}}^{\sigma_p}. \tag{A 8}$$

This results in a growth rate γ for the modes $a_{\boldsymbol{p}}^{\sigma_p}$ and $a_{\boldsymbol{q}}^{\sigma_q}$ given by

$$\gamma^2 = V_{\boldsymbol{p}\,\boldsymbol{k}\,-\boldsymbol{q}}^{\sigma_p\sigma_k\sigma_q} V_{-\boldsymbol{q}\,-\boldsymbol{k}\,\boldsymbol{p}}^{\sigma_p\sigma_k\sigma_q} |a_{\boldsymbol{k}}^{\sigma_k}|^2 \tag{A 9}$$

$$= \frac{1}{64}\frac{(\widehat{\boldsymbol{z}}\cdot(\boldsymbol{p}\times\boldsymbol{q}))^2}{\xi(p_\perp)\xi(q_\perp)}\frac{1}{k_\perp^2 p_\perp^2 q_\perp^2}\left(\frac{\sigma_k}{\xi(q_\perp)} - \frac{\sigma_p}{\xi(k_\perp)}\right)\left(\frac{\sigma_p}{\xi(k_\perp)} - \frac{\sigma_k}{\xi(p_\perp)}\right)$$
$$\times\left(\sigma_k k_\perp^2\xi(k_\perp) + \sigma_p p_\perp^2\xi(p_\perp) + \sigma_q q_\perp^2\xi(q_\perp)\right)^2 |a_{\boldsymbol{k}}^{\sigma_k}|^2, \tag{A 10}$$

where the eigenmode $a_{\boldsymbol{k}}^{\sigma_k}$ satisfies $|a_{\boldsymbol{k}}^{\sigma_k}|^2 = (8/\beta_e)|B_\perp(\boldsymbol{k})|^2$ (Passot & Sulem 2019). Instability thus requires

$$\left(\frac{\sigma_k}{\xi(q_\perp)} - \frac{\sigma_p}{\xi(k_\perp)}\right)\left(\frac{\sigma_p}{\xi(k_\perp)} - \frac{\sigma_k}{\xi(p_\perp)}\right) > 0. \tag{A 11}$$

Equation (7.5) of Voitenko (1998*a*) (see also Zhao *et al.* (2010*b*)) is reproduced when noting that in the latter equation the length unit is not ρ_s but ρ_i defined as $\sqrt{\tau}\rho_s$ and that ξ, defined as the ratio of the Alfvén to the KAW frequency, is independent of the length unit. In the framework of the present paper, the growth rate of the parametric decay instability scales, in the ERMHD regime, as $\gamma \sim k_\perp^2 \beta_e^{-1/2}|B_k|$ when $\beta_e \lesssim 1$ and $\gamma \sim k_\perp^2 \beta_e^{-1}|B_k|$ when $\beta_e \gg 1$ (recall that for $\beta_e \gg 1$, $\xi(k_\perp) = s/v_{ph} \sim \frac{1}{sk_\perp}$). Note that, if we use d_i as length unit, thus writing $k_\perp = (\overline{k}_\perp d_i)/s$, where $\overline{k}_\perp$ denotes the corresponding dimensional wavenumber, the growth rate γ does not scale with β_e in the large β_e limit, as it is the case in EMHD for whistler waves (Zhao *et al.* 2010*a*).

Appendix B. Energy and GCH shell-to-shell transfers

Useful information on the cascade dynamics is provided by analyzing the energy and GCH shell-to-shell transfers in Fourier space, when proceeding as in Alexakis *et al.* (2007) and Mininni *et al.* (2007). As in the calculation of the transverse and parallel energy and GCH spectra, we perform a partition of the Fourier space either in cylindrical shells $S_{K_\perp}$ including all the wavevectors whose transverse component obeys $K_\perp < |\boldsymbol{k}_\perp| \leqslant K_\perp + dk_x$, or in slabs $S_{K_\parallel}$ including all the wavevectors whose parallel component k_z obeys $K_z < |k_z| \leqslant K_z + dk_z$, with the goal to study the perpendicular and parallel transfer respectively. Here, dk_x and dk_z refer to the spectral mesh along the transverse axes and along the parallel axis, respectively.

Our aim is to estimate the energy and GCH transfer rates $T_E(K,P)$ and $T_C(K,P)$), respectively, between a shell K that receives and a shell P that gives, such that it is possible to write $\partial_t E_K = \sum_P T_E(K,P)$ and $\partial_t C_K = \sum_P T_C(K,P)$, where E_K and C_K are the contributions of a cylindrical or of a slab-shaped shell S_K to the energy $\mathcal{E}$ and to the GCH $\mathcal{C}$ respectively ($\mathcal{E} = \sum_K E_K$ and $\mathcal{C} = \sum_K C_K$). Due its physical meaning, we expect that $T_E(P,K) = -T_E(K,P)$ and $T_C(P,K) = -T_C(K,P)$ are antisymmetric, since the amount of the invariant that the K-shell gives to P equals the amount of the same invariant that the P-shell receives. Finally, the total fluxes of energy $\Pi_E(K)$ and GCH $\Pi_C(K)$ through a wavenumber K

$$\Pi_E(K) = -\sum_{K'=0}^{K}\sum_{P=0}^{\infty} T_E\left(K',P\right), \qquad \Pi_C(K) = -\sum_{K'=0}^{K}\sum_{P=0}^{\infty} T_C\left(K',P\right) \tag{B 1}$$

are obtained from the shell-to shell transfer $T_E(K',P)$ or $T_C(K',P)$ by the summing over P and over $K' \leqslant K$.

A scalar field A restricted to a shell S_K (here and in the following K holds for either $K_\perp$ or $K_\parallel$) can be represented in terms of its Fourier modes $\hat{A}_{\boldsymbol{k}}$ by

$$A_K(\boldsymbol{x}) = \sum_{\boldsymbol{k}\in S_K} \widehat{A}_{\boldsymbol{k}} e^{i\boldsymbol{k}\cdot\boldsymbol{x}}, \tag{B 2}$$

so that

$$\sum_K A_K(\boldsymbol{x}) = A(\boldsymbol{x}). \tag{B 3}$$

When considering two scalar fields A and B, one has,

$$\int d^3x A_K(\mathbf{x})B(\mathbf{x}) = \sum_{\mathbf{k}\in S_K^{\pm}} \int d^3x \widehat{A}_{\mathbf{k}} e^{i\mathbf{k}\cdot\mathbf{x}} B(\mathbf{x}) = \frac{1}{(2\pi)^3} \sum_{\mathbf{k}\in S_K^{\pm}} \widehat{A}_{\mathbf{k}} \widehat{B}^{\star}_{\mathbf{k}} \tag{B 4}$$

and

$$\int d^3x A_K(\mathbf{x})B_K(\mathbf{x}) = \sum_{\mathbf{k}\in S_K^{\pm}} \sum_{\mathbf{k}'\in S_K^{\pm}} \int d^3x \widehat{A}_{\mathbf{k}} e^{i(\mathbf{k}+\mathbf{k}')\cdot\mathbf{x}} \widehat{B}_{\mathbf{k}'} = \frac{1}{(2\pi)^3} \sum_{\mathbf{k}\in S_K^{\pm}} \widehat{A}_{\mathbf{k}} \widehat{B}^{\star}_{\mathbf{k}}, \tag{B 5}$$

where again K holds for either $K_\perp$ or $K_\parallel$, depending if perpendicular or parallel transfers are considered. In practice, the latter expression is used to evaluate various integrals arising in the expression of the transfer $T_E(K,P)$ and $T_C(K,P)$.

For the two-fluid gyrofluid, the two-fluid Lie-dragging formulation (2.15) can be conveniently used when electron inertia is retained. The total GCH reads $\mathcal{C} = \int C d^3x$, where we define the GCH density as

$$C = -\frac{1}{4\delta}\left\{(G^+)^2 - (G^-)^2\right\}. \tag{B 6}$$

It follows that

$$\begin{aligned}\partial_t C = \frac{1}{2\delta}\Big\{ & G^+[\varphi^+, G^+] - G^-[\varphi^-, G^-] - \frac{1}{2\delta}\partial_z((G^+)^2 + (G^-)^2) \\ & + \frac{2}{\delta} L_e A_\parallel \partial_z A_\parallel + 2\delta N_e \partial_z (1 - M_1)\varphi\Big\}.\end{aligned} \tag{B 7}$$

To simplify the notation, we will use

$$\sum_{\pm} \pm G^{\pm}[\varphi^{\pm}, G^{\pm}] \equiv G^+[\varphi^+, G^+] - G^-[\varphi^-, G^-].$$

In this case, the contribution $C_K = \int_{S_K} C\, d^3x$ of shell K to GCH ($\mathcal{C} = \sum_K C_K$) obeys

$$\dot{C}_K = \frac{1}{2\delta} \int d^3x \sum_P \sum_{\pm} \pm G_K^{\pm}\left[\varphi^{\pm}, G_P^{\pm}\right], \tag{B 8}$$

where the contribution of the terms involving a z-derivative cancel out by space integration, when using that $N_e = -M_2\varphi$ and the hermiticity of the operators M_1, M_2 and $-\Delta_\perp$. The formulation given by Eq. (B 8) is interesting, since it is as though the transfer is achieved via Lie-drag over the flow corresponding to $\varphi^{\pm}$. In terms of primitive fields, the expression evaluates to

$$\begin{aligned}\dot{C}_K = \frac{1}{2\delta} \int d^3x \sum_P & \left(L_e A_\parallel\right)_K \left[\frac{A_\parallel}{\delta}, \left(L_e A_\parallel\right)_P\right] - \left(L_e A_\parallel\right)_K \left[\left(M_3 - M_2\right)\varphi, \right. \\ & \left. \delta(M_2\varphi)_P\right] - \delta(M_2\varphi)_K \left[\left(M_3 - M_2\right)\varphi, \left(L_e A_\parallel\right)_P\right] + \delta(M_2\varphi)_K \left[\frac{A_\parallel}{\delta}, \delta(M_2\varphi)_P\right].\end{aligned} \tag{B 9}$$

The first summand, which involves a term $A_{\parallel K}[A_\parallel, A_{\parallel P}]/\delta$ has a singular behavior as $\delta \to 0$, but it does not contribute to the flux and is thus physically irrelevant. We will ignore it in the estimate of the shell-to-shell transfer.

Turning to the energy, we write $\mathcal{E} = \sum_K E_K$ where E_K, given by

$$E_K = \frac{1}{2}\int \left\{(M_2\varphi_K)((1 - M_1)\varphi_K) + (M_2\varphi_K)^2 - \frac{2}{\beta_e}(L_e A_K)(\Delta_\perp A_K)\right\} d^3x, \tag{B 10}$$

is the contribution of shell K to the energy. The operator arising in the above equation being hermitian, we can write

$$\partial_t E_K = \int \left\{ ((1-M_1)\varphi_K)\partial_t(M_2\varphi_K) + (M_2\varphi_K)\partial_t(M_2\varphi_K) - \frac{2}{\beta_e}(\Delta_\perp A_K)\partial_t(L_e A_K) \right\} d^3x \tag{B 11}$$

or

$$\partial_t E_K = \int \left\{ ((1-M_1)\varphi_K)\partial_t(M_2\varphi) + (M_2\varphi_K)\partial_t(M_2\varphi) - \frac{2}{\beta_e}(\Delta_\perp A_K)\partial_t(L_e A_) \right\} d^3x,$$

$$\partial_t E_K = \frac{1}{4}\int \Big\{ -(\varphi_K^+ + \varphi_K^-)\partial_t \frac{G^+ - G^-}{\delta} + \frac{G_K^+ - G_K^-}{\delta}\partial_t \frac{G^+ - G^-}{\delta} + \frac{G_K^+ + G_K^-}{\delta}\partial_t \frac{G^+ + G^-}{\delta}$$

$$-(\varphi_K^+ - \varphi_K^-)\partial_t \frac{G^+ + G^-}{\delta} \Big\} d^3x \tag{B 12}$$

where we have replaced L_e by its definition. Equivalently, after a simple algebraic rearrangement,

$$\partial_t E_K = \frac{1}{2\delta}\int \left\{ \left(\frac{G_K^+}{\delta} - \varphi_K^+ \right) \partial_t G^+ + \left(\frac{G_K^-}{\delta} + \varphi_K^- \right) \partial_t G^- \right\} d^3x, \tag{B 13}$$

that we rewrite in the more compact form

$$\partial_t E_K = \frac{1}{2\delta}\int \sum_\pm \left(\frac{G_K^\pm}{\delta} \mp \varphi_K^\pm \right) \partial_t G^\pm \, d^3x. \tag{B 14}$$

We then use the model equations in the form

$$\partial_t G^\pm + [\varphi^\pm, G^\pm \mp \delta\varphi^\pm] + \partial_z(\varphi^\pm \mp \frac{1}{\delta} G^\pm) = 0 \tag{B 15}$$

where we include a additional term in the second argument of the bracket which does not contributes, and get

$$\partial_t E_K = -\frac{1}{2}\int \sum_\pm \left(\frac{G_K^\pm}{\delta} \mp \varphi_K^\pm \right) \left[\varphi^\pm, \frac{G^\pm}{\delta} \mp \varphi^\pm \right] d^3x. \tag{B 16}$$

This enables defining the shell-to-shell energy transfer $T(K,P)$ such that

$$\partial_t E_K = \sum_P T(K,P) \tag{B 17}$$

via

$$T(K,P) = \frac{1}{2}\int \sum_\pm \left(\frac{G_K^\pm}{\delta} \mp \varphi_K^\pm \right) \left[\varphi^\pm, \frac{G_P^\pm}{\delta} \mp \varphi_P^\pm \right] d^3x, \tag{B 18}$$

which is antisymmetric in K and P.

In terms of the primitive variables ($M_3 = 1 + M_2 - M_1$),

$$\left(\frac{G_K^\pm}{\delta} \mp \varphi_K^\pm \right) \left[\varphi^\pm, \frac{G_P^\pm}{\delta} \mp \varphi_P^\pm \right] =$$

$$\left(\mp(M_3\varphi)_K - \frac{2\delta}{\beta_e}\Delta_\perp A_K \right) \left\{ \left[M_3\varphi \pm \frac{1}{\delta} A_\parallel, \mp(M_3\varphi)_P - \frac{2\delta}{\beta_e}\Delta_\perp A_P \right] \right.$$

$$\left. - \left[M_2\varphi \pm \frac{1}{\delta} A_\parallel, \mp(M_3\varphi)_P - \frac{2\delta}{\beta_e}\Delta_\perp A_P \right] \right\} \tag{B 19}$$

includes a term $(M_3\varphi)_K[M_3\varphi, (M_3\varphi)_P]$ that does not contribute to the flux, and that we

thus suppress. As a result, the renormalized transfers we report are calculated according to the formulas

$$T_C(K,P) = \int d^3x \left(\frac{1}{\delta} A_{\parallel K}[A_\parallel, A_{\parallel P}] - \frac{1}{2\delta} \sum_{\pm} \pm G_K^{\pm} \left[\varphi^{\pm}, G_P^{\pm}\right] \right) \tag{B 20}$$

and

$$T_E(K,P) = \int d^3x \left(-(M_3\varphi)_K[(M_3\varphi),(M_3\varphi)_P] - \frac{1}{2} \sum_{\pm} \left(\frac{G_K^{\pm}}{\delta} \mp \varphi_K^{\pm} \right) \left[\varphi^{\pm}, \frac{G_P^{\pm}}{\delta} \mp \varphi_P^{\pm} \right] \right). \tag{B 21}$$

REFERENCES

Abdelhamid, H. M., Lingam, M. & Mahajan, S. M. 2016 Extended MHD turbulence and its applications to the solar wind. *Astrophys. J.* **829**, 87.

Alexakis, A. & Biferale, L. 2018 Cascades and transitions in turbulent flows. *Phys. Reports* **767-769**, 1 – 101, cascades and transitions in turbulent flows.

Alexakis, A., Bigot, B., Politano, H. & Galtier, S. 2007 Anisotropic fluxes and nonlocal interactions in magnetohydrodynamic turbulence. *Phys. Rev. E* **76**, 056313.

Alexakis, A., Mininni, P. D. & Pouquet, A. 2006 On the inverse cascade of magnetic helicity. *Astrophys. J* **640**, 335–343.

Alexandrova, O. 2008 Solar wind vs magnetosheath turbulence and Alfvén vortices. *Nonlin. Proc. Geophys.* **15** (1), 95–108.

Alexandrova, O., Saur, J., Lacombe, C., Mangeney, A., Mitchell, J., Schwartz, S. J. & Robert, P. 2009 Universality of solar-wind turbulent spectrum from MHD to electron scales. *Phys. Rev. Lett.* **103** (16), 165003.

Balsara, D. & Pouquet, A. 1999 The formation of large-scale structures in supersonic magnetohydrodynamic flows. *Phys. Plasmas* **6** (1), 89–99.

Belcher, J. W. & Davis, Jr., L. 1971 Large-amplitude Alfvén waves in the interplanetary medium, 2. *J. Geophys. Res.* **76**, 3534.

Benavides, S. Jose & Alexakis, A. 2017 Critical transitions in thin layer turbulence. *J. Fluid Mech.* **822**, 364–385.

Biskamp, D., Schwarz, E., Zeiler, A., Celani, A. & Drake, J. F. 1999 Electron magnetohydrodynamic turbulence. *Phys. Plasmas* **6**, 751–758.

Boldyrev, S., Horaites, K., Xia, Q. & Perez, J.C. 2013 Toward a theory of astrophysical plasma turbulence at subproton scales. *Astrophys. J.* **777**, 41.

Brandenburg, A. 2001 The inverse cascade and nonlinear alpha-effect in simulations of isotropic helical hydromagnetic turbulence. *Astrophys. J.* **550** (2), 824–840.

Brandenburg, A. & Matthaeus, W. H. 2004 Magnetic helicity evolution in a periodic domain with imposed field. *Phys. Rev. E* **69**, 056407.

Bruno, R., Telloni, D., DeIure, D. & Pietropaolo, E. 2017 Solar wind magnetic field background spectrum from fluid to kinetic scales. *Month. Not. R. Astro. Soc.* **472**, 1052–1059.

Bruno, R., Trenchi, L. & Telloni, D. 2014 Spectral Slope Variation at Proton Scales from Fast to Slow Solar Wind. *Astrophys. J. Lett.* **793** (1), L15.

Cerri, S. S. & Califano, F. 2017 Reconnection and small-scale fields in 2d-3v hybrid-kinetic driven turbulence simulations. *New J. Phys.* **19**, 025007.

Chen, C. H. K., Bale, S. D., Bonnell, J. W., Borovikov, D., Bowen, T. A., Burgess, D., Case, A. W., Chandran, B. D. G., de Wit, T. Dudok, Goetz, K., Harvey, P. R., Kasper, J. C., Klein, K. G., Korreck, K. E., Larson, D., Livi, R., MacDowall, R. J., Malaspina, D. M., Mallet, A., McManus, M. D., Moncuquet, M., Pulupa, M., Stevens, M. L. & Whittlesey, P. 2020 The evolution and role of solar wind turbulence in the inner heliosphere. *Astrophys. J. Suppl.* **246** (2), 53.

Chen, C. H. K. & Boldyrev, S. 2017 Nature of kinetic scale turbulence in the Earth's magnetosheath. *Astrophys. J.* **842**, 122.

D'Amicis, R., Matteini, L. & Bruno, R. 2019 On the slow solar wind with high Alfvénicity: from composition and microphysics to spectral properties. *Month. Not. R. Astro. Soc.* **483**, 4665–4677.

Del Zanna, L., Velli, M. & Londrillo, P. 2001 Parametric decay of circularly polarized Alfvén waves: Multidimensional simulations in periodic and open domains. *Astron. & Astrophys.* **367**, 705–718.

Fjørtoft, R. 1953 On changes in the spectral distribution of kinetic energy for two-dimensional nondivergent flow. *Tellus* **5**, 225.

Franci, L., Cerri, S. S., Califano, F., Landi, S., Papini, E., Verdini, A., Matteini, L., Jenko, F. & Hellinger, P. 2017 Magnetic Reconnection as a Driver for a Sub-ion-scale Cascade in Plasma Turbulence. *Astrophys. J. Lett.* **850**, L16, arXiv: 1707.06548.

Frisch, U., Pouquet, A., Léorat, J. & Mazure, A. 1975 Possiblility of an inverse cascade of magnetic helicity in magnetohydrodynamic turbulence. *J. Fluid Mech.* **68**, 769–778.

Fu, X., Li, H., Guo, F., Li, X. & Roytershteyn, V. 2018 Parametric Decay Instability and Dissipation of Low-frequency Alfvén Waves in Low-beta Turbulent Plasmas. *Astrophys. J.* **855** (2), 139.

Galtier, S. & Meyrand, R. 2015 Entanglement of helicity and energy in kinetic Alfvén wave/whistler turbulence. *J. Plasma Phys.* **81**, 325810106.

He, J., Duan, D., Zhu, X., Yan, L. & Wang, L. 2019 Observational evidences of wave excitation and inverse cascade in a distant earth foreshock region. *Science China: Earth Sciences* **62**, 619–630.

Howes, G. G., Cowley, S. C., Dorland, W., Hammett, G. W., Quataert, E. & Schekochihin, A. A. 2006 Astrophysical gyrokinetics: Basic equations and linear theory. *Astrophys. J.* **651** (1), 590–614.

Jovanović, Dušan, Alexandrova, Olga, Maksimović, Milan & Belić, Milivoj 2020 Fluid Theory of Coherent Magnetic Vortices in High-β Space Plasmas. *Astrophys. J.* **896** (1), 8.

Kim, H. & Cho, J. 2015 Inverse cascade in imbalanced electron magnetohydrodynamic turbulence. *Astrophys. J.* **801**, 75.

Linkmann, M. & Dallas, V. 2016 Large-scale dynamics of magnetic helicity. *Phys. Rev. E* **94**, 053209.

Linkmann, M. & Dallas, V. 2017 Triad interactions and the bidirectional turbulent cascade of magnetic helicity. *Phys. Rev. Fluids* **2**, 054605.

Lucek, E. A. & Balogh, A 1998 The identification and characterization of Alfvénic fluctuations in Ulysses data at midlatitudes. *Astrophys. J.* **507**, 984–990.

Marino, R., Mininni, P. D., Rosenberg, D. & Pouquet, A. 2013 Inverse cascades in rotating stratified turbulence: Fast growth of large scales. *EPL (Europhysics Letters)* **102** (4), 44006.

Maron, J. & Goldreich, P. 2001 Simulations of Incompressible Magnetohydrodynamic Turbulence. *Astrophys. J.* **554** (2), 1175–1196.

Marsch, E. & Tu, C.-Y. 1990 On the radial evolution of MHD turbulence in the inner heliosphere. *J. Geophys. Res.* **95 (A6)**, 8211–8229.

Matthaeus, W. H. & Goldstein, M. L. 1982 Measurement of the rugged invariants of magnetohydrodynamic turbulence in the solar wind. *J. Geophys. Res.: Space Phys.* **87**, 6011–6028.

Meneguzzi, M., Frisch, U. & Pouquet, A. 1981 Helical and non helical tubulent dynamo. *Phys. Rev. Lett.* **47**, 1660–1664.

Miloshevich, G., Lingam, M. & Morrison, P. J. 2017 On the structure and statistical theory of turbulence of extended magnetohydrodynamics. *New J. Phys.* **19**, 015007.

Miloshevich, G., Passot, T. & Sulem, P. L. 2019 Modeling imbalanced collisionless alfvén wave turbulence with nonlinear diffusion equations. *Astrophys. J.* **888**, L7.

Mininni, P. D., Alexakis, A. & Pouquet, A. 2007 Energy transfer in hall-mhd turbulence: cascades, backscatter, and dynamo action. *JPP* **73** (3), 377–401.

Müller, W-C, Malapaka, S. K. & Busse, A. 2012 Inverse cascade of magnetic helicity in magnetohydrodynamic turbulence. *Phys. Rev. E* **85**, 015302(R).

Nazarenko, S. 2011 *Wave turbulence*, *Lectures Notes in Physics*, vol. 825. Springer.

Passot, T., Sulem, P.L. & Tassi, E. 2018 Gyrofluid modeling and phenomenology of low-β_e Alfvén wave turbulence. *Phys. Plasmas* **25**, 042107.

Passot, T. & Sulem, P. L. 2019 Imbalanced kinetic alfvén wave turbulence: from weak turbulence theory to nonlinear diffusion models for the strong regime. *J. Plasma Phys.* **85**, 905850301.

Perrone, D., Alexandrova, O., Roberts, O. W., Lion, S., Lacombe, C., Walsh, A., Maksimovic, M. & Zouganelis, I. 2017 Coherent Structures at Ion Scales in Fast Solar Wind: Cluster Observations. *Astrophys. J.* **849** (1), 49.

Petviashvili, V. & Pokhotelov, O. 1992 *Solitary Waves in Plasmas and in the Atmosphere*. Philadelphia, PA: Gordon and Breach.

Podesta, J. J. 2013 Evidence of kinetic Alfvén waves in the solar wind at 1 AU. *Solar Phys.* **286**, 529–548.

Pouquet, A., Frisch, U. & Leorat, J. 1976 Strong MHD helical turbulence and the nonlinear dynamo effect. *J. Fluid Mech.* **77**, 321–354.

Pouquet, A., Rosenberg, D., Stawarz, J.E. & Marino, R. 2019 Helicity dynamics, inverse, and bidirectional cascades in fluid and magnetohydrodynamic turbulence: A brief review. *Earth and Space Science* **6**, 351–369.

Pouquet, A., Stawarz, J. E. & Rosenberg, D. 2020 Coupling Large Eddies and Waves in Turbulence: Case Study of Magnetic Helicity at the Ion Inertial Scale. *Atmosphere* **11** (2), 203.

Réville, V., Velli, M., Panasenco, O., Tenerani, A., Shi, C., Badman, S. T., Bale, S. D., Kasper, J. C., Stevens, M. L., Korreck, K. E., Bonnell, J. W., Case, A. W., de Wit, T. Dudok, Goetz, K., Harvey, P. R., Larson, D. E., Livi, R., Malaspina, D. M., MacDowall, R. J., Pulupa, M. & Whittlesey, P. L. 2020 The role of alfvén wave dynamics on the large-scale properties of the solar wind: Comparing an MHD simulation with parker solar probe e1 data. *Astrophys. J. Suppl.* **246** (2), 24.

Roberts, D. A., Goldstein, M. L., Klein, L. W. & Matthaeus, W. H. 1987 Origin and evolution of fluctuations in the solar wind: Helios observations and Helios-Voyager comparisons. *J. Geophys. Res.: Space Physics* **92** (A11), 12023–12035.

Sahraoui, F., Goldstein, M. L., Belmont, G., Canu, P. & Rezeau, L. 2010 Three dimensional anisotropic k spectra of turbulence at subproton scales in the solar wind. *Phys. Rev. Lett.* **105**, 131101.

Salem, C. S., Howes, G. G., Sundkvist, D., Bale, S. D., Chaston, C. C., Chen, C. H. K. & Mozer, F. S. 2012 Identification of kinetic Alfvén wave turbulence in the solar wind. *Astrophys. J. Lett.* **745**, L9.

Schekochihin, A. A., Cowley, S. C., Dorland, W., Hammett, G. W., Howes, G. G., Quataert, E. & Tatsuno, T. 2009 Astrophysical gyrokinetics: kinetic and fluid turbulent cascades in magnetized weakly collisional plasmas. *Astrophys. J. Suppl.* **182**, 310–377.

Seshasayanan, K., Benavides, S. J. & Alexakis, A. 2014 On the edge of an inverse cascade. *Phys. Rev. E* **90**, 051003.

Shi, M., Li, H., Xiao, C. & Wang, X. 2017 The Parametric Decay Instability of Alfvén Waves in Turbulent Plasmas and the Applications in the Solar Wind. *Astrophys. J.* **842** (1), 63.

Shoda, M. & Yokoyama, T. 2018 Anisotropic magnetohydrodynamic turbulence driven by parametric decay instability: The onset of phase mixing and alfvén wave turbulence. *Astrophys. J.* **859** (2), L17.

Slepyan, L. I. 2015 On the energy partition in oscillations and waves. *Proc. R. Soc. A* **471**, 20140838.

Solano, E. R., Lomas, P. J., Alper, B., Xu, G. S., Andrew, Y., Arnoux, G., Boboc, A., Barrera, L., Belo, P., Beurskens, M. N. A., Brix, M., Crombe, K., de la Luna, E., Devaux, S., Eich, T., Gerasimov, S., Giroud, C., Harting, D., Howell, D., Huber, A., Kocsis, G., Korotkov, A., Lopez-Fraguas, A., Nave, M. F. F., Rachlew, E., Rimini, F., Saarelma, S., Sirinelli, A., Pinches, S. D., Thomsen, H., Zabeo, L. & Zarzoso, D. 2010 Observation of confined current ribbon in jet plasmas. *Phys. Rev. Lett.* **104**, 185003.

Stribling, T., Matthaeus, W. H. & Ghosh, S. 1994 Nonlinear decay of magnetic helicity in magnetohydrodynamic turbulence with a mean magnetic field. *J. Geophys. Res.: Space Phys.* **99**, 2567–2576.

Tassi, E., Passot, T. & Sulem, P. L. 2020 A Hamiltonian gyrofluid model based on a quasi-static closure. *J. Plasma Phys.* In press.

Tu, C. Y., March, E. & Rausenbauer, H. 1990 The dependence of MHD turbulence spectra on the inner solar wind stream structure near solar minimum. *Geophys. Res. Lett.* **17**, 283–286.

Tu, C.-Y., Marsch, E. & Thieme, K. M. 1989 Basic properties of solar wind MHD turbulence near 0.3 AU analyzed by means of elsasser variables. *J. Geophys. Res.* **94 (A9)**, 11739–11759.

Viñas, A. F. & Goldstein, M. L. 1991 Parametric instabilities of circularly polarized large-amplitude dispersive Alfvén waves: excitation of obliquely-propagating daughter and side-band waves. *J. Plasma Phys.* **46**, 129–152.

Voitenko, Y. M. 1998*a* Three-wave coupling and parametric decay of kinetic Alfvén waves. *J. Plasma Phys.* **60**, 497–514.

Voitenko, Y. M. 1998*b* Three-wave coupling and weak turbulence of kinetic Alfvén waves. *J. Plasma Phys.* **60**, 515–527.

Wang, T., Alexandrova, O., Perrone, D., Dunlop, M., Dong, X., Bingham, R., Khotyaintsev, Y. V., Russell, C. T., Giles, B. L., Torbert, R. B., Ergun, R. E. & Burch, J. L. 2019 Magnetospheric Multiscale Observation of Kinetic Signatures in the Alfvén Vortex. *Astrophys. J. Lett.* **871** (2), L22.

Wicks, R. T., Roberts, D. A., Mallet, A., Schekochihin, A. A., Horbury, T. S. & Chen, C. H. K. 2013 Correlations at large scales and the onset of turbulence in the fast solar wind. *Astrophys. J.* **778**, 177.

Zakharov, V. E., L'Vov, V. S. & Falkovich, G. 1992 *Kolmogorov spectra of turbulence I: Wave turbulence*. Springer Series in Nonlinear Dynamics.

Zhao, J. S., Lu, J. Y. & Wu, D. J. 2010*a* Parametric instability of whistler waves in the electron magnetohydrodynamics. *Astrophys. J.* **714**, 138–143.

Zhao, J. S., Wu, D. J. & Lu, J. Y. 2010*b* On nonlinear decay of kinetic Alfvén waves and application to some processes in space plasmas. *J. Geophys. Res.: Space Phys.* **115**, A12227.

Zhou, M., Loureiro, N. F. & Uzdensky, D. A. 2020 Multi-scale dynamics of magnetic flux tubes and inverse magnetic energy transfer. *J. Plasma Phys.* **86**, 535860401.

Zocco, A. & Schekochihin, A. A. 2011 Reduced fluid-kinetic equations for low-frequency dynamics, magnetic reconnection, and electron heating in low-beta plasmas. *Phys. Plasmas* **18**, 102309.